MR. DANIEL COLLINS (Orcid ID : 0000-0002-3183-2825)

DR. JON HILL (Orcid ID : 0000-0003-1340-4373)

Article type : Original Manuscript

Controls on tidal sedimentation and preservation: Insights from numerical tidal modelling in the Late Oligocene–Miocene South China Sea, Southeast Asia

DANIEL S. COLLINS[1*], ALEXANDROS AVDIS[1], PETER A. ALLISON[1], HOWARD D. JOHNSON[1], JON HILL[2] and MATTHEW D. PIGGOTT[1]

[1] *Department of Earth Science and Engineering, Imperial College London, South Kensington Campus, London, SW7 2AZ UK*

[2] *Environment Department, University of York, Heslington, York, YO10 5DD UK*

*corresponding author: dscollins.geo@gmail.com

Associate Editor – J P Walsh

Short Title – Controls on tidal sedimentation and preservation

ABSTRACT

Numerical tidal modelling, when integrated with other geological datasets, can significantly inform the analysis of physical sedimentation processes and the depositional and preservational record of ancient tide-influenced shoreline–shelf systems. This is illustrated in the Oligo–Miocene of the South China Sea, which experienced significant changes in basin physiography and where tide-influenced, shoreline–shelf deposition is preserved in *ca* 10 sub-basins. Palaeogeographic reconstructions, palaeotidal modelling and regional sedimentary facies analysis have been integrated in order to evaluate the spatial–temporal evolution and physiographic controls on tidal sedimentation and preservation during the *ca* 25 Myr Oligo–Miocene record in the South China Sea. Palaeotidal modelling, using an astronomically-forced and global tidal model (Fluidity) at a maximum 10 km resolution, indicates that spring tides along Late Oligocene to Middle Miocene coastlines were predominantly mesotidal–macrotidal and capable of transporting sand, which reflects two main conditions: (i) increased tidal inflow through wider ocean connections to the Pacific Ocean; and (ii) tidal amplification resulting from constriction of the tidal wave in a 'blind gulf' type of basin morphology. Since the Middle to Late Miocene, a reduction in the amplitude and strength of tides in the South China Sea was mainly due to diminishing tidal inflow from the Pacific Ocean caused by the northward movement of the Philippines and Izu–Bonin–Mariana arc. Sensitivity tests to palaeogeographic and palaeobathymetric uncertainty indicate that regional-scale (hundreds to thousands of kilometres) palaeogeographic changes influencing tidal inflow versus outflow can

override local-scale (one to hundreds of kilometres) changes to tidal resonance and convergence effects (funnelling and shoaling), such as shelf width and shoreline geometry. Palaeotidal model results compare favourably to the distribution and sedimentary fabric of Oligo–Miocene, tide-influenced, shoreline–shelf successions in peripheral South China Sea basins. However, the preservation potential of tidal deposits is lower in open coastline environments, probably due to enhanced reworking during storms and river floods.

Keywords: Embayments, numerical modelling, Oligocene–Miocene, preservation, shoreline–shelf, South China Sea, tidal amplification, tides

INTRODUCTION

The stratigraphic record is a consequence of the integration between deposition and preservation. In shoreline–shelf systems, deposition results from the interaction of episodic tidal, fluvial, wave and storm processes (e.g. Coleman and Wright, 1975; Galloway, 1975; Ainsworth et al., 2011). However, these processes have different preservation potential because they operate on varying timescales and are associated with different sedimentation rates and deposit thicknesses (Fig. 1) (e.g. Miall, 2015). Higher magnitude-lower frequency processes (for example, infrequent fluvial floods and storms) have a higher preservation potential on a thousand-year timescale (Fig. 1) because these events: (i) erode the deposits of lower magnitude–high frequency processes; and (ii) form thicker deposits that minimize physical and biological reworking, including complete bioturbation, before the succeeding event (e.g. Dott, 1983; Thorne et al., 1991; Wheatcroft and Drake, 2003; Miall, 2015). Longer-term ($\geq 10^3$ year) preservation requires the rates of accommodation creation and burial due to autogenic processes (for example, distributary channel switching), orbital-forced processes (for example, nodal channel avulsion) and tectonics (Fig. 1), to exceed the rate of erosion and biogenic reworking (e.g. Miall, 2015). Consequently, stratigraphy is inherently fragmentary (e.g. Barrell, 1917; Dott, 1983; Plotnick, 1986; Ager, 1993) and records repeated episodes of deposition and repeated *accidents* of preservation (e.g. Sadler, 1981; Miall, 2015).

Ancient tide-dominated successions (e.g. Nio and Yang, 1991; Davis and Dalrymple, 2011; Longhitano et al., 2012; Plink-Björklund, 2012) commonly record deposition in the following settings: (i) shoreline–shelf embayments, estuaries or straits during transgression (e.g. Van Wagoner, 1991; Posamentier and Allen, 1999); (ii) shorelines, including deltas, that are undergoing regression (e.g. Martinius et al., 2001; Legler et al., 2013; van Cappelle et al., 2017) or aggradation (e.g. Olariu et al., 2012); (iii) along various types of coastline adjacent to wide (>75 km) shelves (e.g. Ainsworth et al., 2015); and (iv) shoreline–shelf embayments in association with wide shelves (or seaways) (e.g. Steel et al., 2012; Chen et al., 2014). These depositional settings are consistent with observations from present-day tide-dominated systems; the highest tidal ranges on Earth occur in coastal embayments, while tide-dominated coastlines typically occur where adjacent shelf widths (perpendicular to the coastline) exceed 75 km (Ainsworth et al., 2011). Consequently, shoreline geometry and wide shelves (>75 km) are widely interpreted to be one of the foremost palaeogeographic controls on tide-influenced deposition, including process-based classification schemes of ancient coastal–deltaic to shallow marine deposits (Ainsworth et al., 2011; Vakarelov and Ainsworth, 2013).

Palaeotidal modelling enables quantitative assessment of tides along ancient coastlines and can test their sensitivity to different palaeogeographic and palaeobathymetric configurations, including coastal rugosity, shelf width and basin physiography (geometry and bathymetry) (Wells et al., 2005a; Wells et al., 2005b; Wells et al., 2007a; Wells et al., 2007b; Mitchell et al., 2010; Wells et al., 2010a; Wells et al., 2010b; Mitchell et al., 2011). Ancient tidal modelling has advanced since early approaches (e.g. Slingerland, 1986), but simulations have only investigated tidal amplitude (Slingerland, 1986; Wells et al., 2005a; Wells et al., 2005b; Wells et al., 2007a; Wells et al., 2010a; Wells et al., 2010b) and bed shear stress (Mitchell et al., 2010; Mitchell et al., 2011) in ancient epicontinental seaways. Furthermore, since the initial palaeotidal modelling studies, there have been improvements in current understanding of shoreline–shelf process classification (Ainsworth et al., 2011; Vakarelov and Ainsworth, 2013), the recognition of ancient mixed-process stratigraphy (MacEachern and Bann, 2008; Ainsworth et al., 2011; Buatois et al., 2012; Rossi and Steel, 2016; van Cappelle et al., 2016), and the controls on tide, wave and fluvial processes (Ainsworth et al., 2011; Nyberg and Howell, 2016).

The South China Sea (SCS) region in Southeast Asia (Fig. 2) is tectonically active, with significant plate tectonic changes since the Oligocene (e.g. Longley, 1997; Hall, 2002; Morley, 2016). Tectonics and thermal subsidence caused significant (>4 to 5 km) subsidence and preservation of Oligo–Miocene, shoreline–shelf successions in several SCS basins (Longley, 1997; Doust and Sumner, 2007; Morley, 2016), many of which show evidence of tidal influence (Collins et al., 2017a).

The main aim of this paper is to use palaeotidal modelling to understand the impact of tectonic-driven physiographic changes on shoreline–shelf tides and stratigraphic preservation. The objectives of this paper are to: (i) reconstruct a time-series of Oligo–Miocene palaeogeographies (specifically palaeocoastlines and palaeobathymetries) of the SCS region and use tidal modelling to assess the impact of palaeogeographic changes and uncertainty on tidal processes; (ii) compare tidal model results to sedimentary facies and biostratigraphic data from Oligo–Miocene successions in and around the SCS; and (iii) evaluate the tectono-physiographic controls on tidal processes in a region that has undergone significant, tectonically-induced basin modifications during the *ca* 25 Myr period of investigation.

LATE OLIGOCENE–MIOCENE PALAEOGEOGRAPHY OF THE SOUTH CHINA SEA

Methods

Seven highstand palaeogeographic and palaeobathymetric reconstructions for the SCS region (Figs 3 and 4) were generated for Late Oligocene (26 Ma), Early Miocene (21 Ma and 18 Ma), Middle Miocene (15 Ma and 12 Ma) and Late Miocene (11 Ma and 6 Ma) timeslices (Markwick and Valdes, 2004) using the Getech plate model and synthesising sedimentological, stratigraphic, biostratigraphic and palaeogeographic data (Fig. 5) (e.g. Longley, 1997; Hall, 2002; Doust and Sumner, 2007; Shoup et al., 2013). The Getech plate model is a global model that defines palaeoplate boundaries based on presently observable structures and assumes that these

boundaries remain unchanged throughout geological time (rigid plate model) (Mazur et al., 2012). Plate positions were constrained using: (i) magnetic ocean floor anomalies; (ii) palaeomagnetic data; and (iii) geological and geophysical evidence (Mazur et al., 2012). Oligo–Miocene spatio-temporal changes in shoreline–shelf sedimentation, stratigraphic architecture and physiography were caused by variations in tectonic subsidence and inversion, thermal subsidence, sediment supply and global eustatic sea level (Fig. 5). Ocean crust bathymetry was calculated by applying an age-depth relationship (Stein and Stein, 1992) to a rotated ocean age dataset (Müller et al., 1997) which was corrected for sediment cover, sea-level changes and oceanic seamount intrusion (Markwick and Valdes, 2004). The boundaries between gross depositional environments (Fig. 3) were extracted as palaeobathymetric contours and interpolated to form a palaeobathymetric grid with a 0.1° (*ca* 10 km) resolution (Fig. 4). The SCS reconstructions were included in global palaeogeographic reconstructions generated by Getech Globe (http://www.getech.com/globe/).

Summary of palaeogeographic evolution

The SCS study area is bounded by the Indo-Australian and Eurasian plates and by the Pacific-Philippine Sea (Fig. 2). Present-day seismicity and GPS measurements indicate high tectonic activity (Simons et al., 2007) and a complex arrangement of microplates and sub-plates, which have undergone substantial, and relatively rapid, reorganization during the Oligocene–Present (Hall, 2002).

In the Early–Late Oligocene, the slab-pull effect due to subduction of the proto-SCS beneath north-west Borneo caused rifting along southern China (Fig. 3) (Holloway, 1982; Taylor and Hayes, 1983; Hall, 2002). Furthermore, tectonic extrusion related to collision between the India and Eurasia plates resulted in sinistral displacement along several major north-west/south-east faults, such as the Ailao Shan–Red River Fault Zone (Fig. 3) (e.g. Tapponnier et al., 1986; Replumaz and Tapponnier, 2003). The combined effect of slap-pull and tectonic extrusion initiated sea floor spreading in the SCS at *ca* 32 Ma (Briais et al., 1993; Barckhausen et al., 2014) or 31 Ma (Barckhausen and Roeser, 2004).

During the Oligocene–Miocene, clockwise rotation and northward translation of the Philippine Sea Plate (Hall et al., 1995; Hall, 2002; Gaina and Müller, 2007) and related tectonic deformation caused the gradual narrowing of the Luzon Strait and the complex assembly of the present-day Philippine islands by the Middle–Late Miocene (Figs 3 and 4). Furthermore, northward movement of the Philippine Sea Plate was accompanied by rifting and subsequent oceanic spreading along its eastern margin, which caused narrowing of the connection to the Pacific Ocean north of the Izu–Bonin–Mariana (IBM) arc (Fig. 4).

By the Early–Middle Miocene, the proto-SCS was almost completely closed (Figs 3B, 3C and 4B to D) and extended continental crust from the rifted South China margin was being subducted under Borneo (Taylor and Hayes, 1983; Hall, 2002; Hutchison, 2010). The precise timing of initial collision is uncertain, not least because it is diachronous and spatially variable (for example, propagating from

south-west to north-east along north-west Borneo). Subduction-related deformation is interpreted to form the Base Miocene (*ca* 23 Ma) (Balaguru and Hall, 2008), Deep Regional (*ca* 17 to 15 Ma) and other regional unconformities (e.g. Levell, 1987; Hazebroek and Tan, 1993) in offshore Sabah. Underthrusting terminated subduction and was followed by uplift, crustal shortening and widespread shoreline–shelf deposition. By the Late Miocene, a foredeep trough had formed along north-west Borneo (Figs 3 and 4) (Hinz et al., 1989; Hall, 2002; Ingram et al., 2004; Franke et al., 2008; Hutchison, 2010).

Oceanic spreading in the SCS ceased at either 20.5 Ma (Barckhausen and Roeser, 2004) or 15.0 Ma (Briais et al., 1993). Tectonic flow lines produced by a plate model using the Briais et al. (1993) interpretation are consistent with the trend of ocean floor fracture zones (Mazur et al., 2012), whereas the *ca* 32.0 to 20.5 Ma spreading model of Barckhausen et al. (2014) has not been tested. The present study uses the Briais et al. (1993) model (Fig. 3) (Mazur et al., 2012).

The Sunda Shelf was emergent throughout the Oligo–Miocene, creating a 'blind gulf'-type of basin morphology (Fig. 4A to G), which was only breached in the Holocene and persists to the present-day (Fig. 4H) (van Hattum et al., 2006; Hall, 2013; Shoup et al., 2013). The size and depth of the Gulf of Thailand (Fig. 2) have increased since its initial formation in the Late Oligocene–Early Miocene, due to tectonic extension and eustatic sea-level rise (Figs 3 and 4) (Miller et al., 2011). Since the Middle–Late Miocene thermal subsidence and eustatic sea-level rise has caused further marine transgression into the Gulf of Thailand (Figs 4D to G and 5) (Doust and Sumner, 2007; Miller et al., 2011; Shoup et al., 2013). The Natuna Arch, which separates the East and West Natuna basins (Fig. 2), was a tectonic high throughout the Oligocene–early Late Miocene (Fig. 3A to F) (Shoup et al., 2013).

Palaeogeographic uncertainty

Sensitivity tests of the tidal model were performed on the 'base-case' palaeogeographies (Figs 3 and 4) to investigate the effect on tides of three principal palaeogeographic uncertainties: (i) eustatic sea-level lowstand; (ii) palaeogeographic positioning of Palawan; and (iii) palaeobathymetry of the IBM arc.

Eustatic sea-level lowstand

Global eustatic sea-level changes during the Late Oligocene–Miocene were approximately 50 m (Miller et al., 2011). Consequently, sensitivity tests of tidal models were performed for palaeobathymetric reconstructions with a 50 m lower sea level (lowstand) (Supporting Fig. 1).

Palaeogeographic positioning of Palawan

Palawan (Fig. 2) was attached to South China until the Eocene (Holloway, 1982; Almasco et al., 2000; Suzuki et al., 2000) and two tectonic models have been proposed for the Oligocene–Middle Miocene: Model 1 – Palawan was located along the northern margin of the proto-SCS and rifted from South China during opening of the SCS (Fig. 3A to C) (Holloway, 1982; Hall, 2002; Hall, 2012); and Model 2 – Palawan was located on the southern margin of the proto-SCS and rifted from South

China during opening of the proto-SCS (Hutchison, 2010; Morley, 2012). Both of these models are plausible because the preserved stratigraphy from the proto-SCS is equivocal, there is no consensus on the origin of ophiolites in the Philippines (e.g. Aurelio et al., 2014; Morley, 2016) and a foredeep origin for the north-west Borneo–Palawan Trough is possible in both models (Morley, 2016). Base-case palaeogeographies favour Model 1 (Figs 3A to C) (Mazur et al., 2012). Sensitivity tests were performed on Late Oligocene–Early Miocene 'base-case' palaeogeographies but with Palawan submerged to 10 m water depth (Fig. 3H to J), which was limited by the methodology for editing the palaeobathymetric mesh. The lack of an emergent Palawan along the northern SCS margin approximates Model 2 but a more thorough sensitivity test requires modification to the plate model.

Palaeobathymetry of the Izu–Bonin–Mariana (IBM) arc

Throughout the Oligo–Miocene, the IBM volcanic arc was located along the Philippine Sea and Pacific plate boundary (Fig. 4) but the palaeobathymetry of the IBM arc is uncertain. The IBM arc is modelled as emergent in the base-case palaeogeographic interpretations. However, this is an unrealistic end-member palaeogeographic interpretation that is hypothesized to produce an extreme blocking effect on tides entering the SCS from the Pacific Ocean. Hence, the base-case tidal models are hypothesized to indicate a minimum tidal potential in the SCS because more tidal energy is likely to have propagated between islands in the volcanic arc. A sensitivity test was performed for a 6 Ma base-case palaeogeography in which the IBM arc was submerged to a depth of 10 m, as limited by the methodology for editing the palaeobathymetric mesh. A 10 m submerged depth does not capture the full range of uncertainty but is hypothesized to permit a relative increase in tidal throughflow sufficient to indicate the sensitivity of tides to the palaeobathymetry of the IBM arc.

PALAEOTIDAL MODELLING

Model setup

Fluidity (http://fluidityproject.github.io/) is a hydrodynamic, finite element ocean model that uses unstructured, tetrahedral meshes to maximise computational accuracy and efficiency (Wells et al., 2005a; Piggott et al., 2008; Geuzaine and Remacle, 2009). Multi-scale, three-dimensional, global computational meshes produced using 'qmsh' (Avdis et al., 2018) have the highest mesh resolution of *ca* 10 km in areas of complex bathymetry. A minimum depth (10 m) along the coastline prevents the free surface from intersecting the bottom surface as it propagates (e.g. Wells et al., 2010a). Simulations are global, without data assimilation and represent full astronomical tidal forcing for three-months simulation time and a spin-up period of 120 hours simulation time, which is sufficient to remove spin-up effects and reach steady state (Wells et al., 2007a; Wells et al., 2007b). The equations of motion describing the movement of the tidal bulge include the Coriolis acceleration (f), which is simplified to $f = 2\Omega \sin \phi$ (Cushman-Roisin and Beckers, 2011), where Ω is the rotation rate of the Earth ($7.27 \times 10 - 5$ rad s^{-1}) and ϕ is the latitude.

Model outputs are the amplitude of tidal components, tidal range, average and maximum tidal current velocity, the magnitude and direction of average and maximum tidal bed shear stress, and the tidal phase. Tidal range is calculated as the difference between the maximum and minimum free

surface heights over the post spin-up simulation period, which approximately equals the maximum spring tidal range. The amplitude and phase of the four major tidal constituents (M_2, S_2, K_1 and O_1) are determined using tidal harmonic analysis of the modelled time series of free surface heights (Foreman, 1979).

Tidal bed shear stress (τ) is the frictional force exerted by tides on the sediment surface and is calculated using:

$$\tau = \rho C_D |\bar{u}|\bar{u} \quad (1)$$

where ρ = the density of water (1023 kg m^{-3}), C_D = is the drag coefficient, and $|\bar{u}|$ is the depth averaged current velocity ($|\bar{u}| = \sqrt{u^2 + v^2 + w^2}$, where *u*, *v* and *w* represent the velocities in the x, y, and z dimensions, respectively, in ms^{-1}) (Pingree and Griffiths, 1979; Wells et al., 2007a; Mitchell et al., 2010). The drag coefficient is taken as 0.0025, a generic value used in most ocean models (Pietrzak et al., 2002), but the drag coefficient may vary between 10^{-2} and 10^{-3} as a function of bathymetry and sediment grain size, shape and sorting (Safak, 2016). Bed shear stress magnitudes can be converted to the equivalent grain size that could be entrained by the tidal flow based on the modelled and calculated critical bed shear stress values for sediment transport (Miller et al., 1977; Soulsby et al., 1993; Julien and Raslan, 1998).

Tidal resonance and convergence effects

Tides in shelf and shoreline regions may undergo amplification due to convergence. This comprises the transformation of tidal waves due to shoaling and bathymetric constriction, and resonance, which occurs when the natural period of oscillation on the shelf or within a shoreline–shelf embayment is coincident with the tidal period (Slingerland, 1986; Allen, 1997).

Convergence effects (funnelling and shoaling) are estimated by:

$$\frac{A_e}{A_o} = \left(\frac{w_o}{w_e}\right)^{1/2} \left(\frac{h_o}{h_e}\right)^{1/4} \quad (2)$$

where *A*= tidal range (m), *w* = water body width (m) and *h* = water body depth (m). Subscript 'o' denotes the open, deeper water body and subscript 'e' the narrower, shallower water body (Slingerland, 1986). The convergence effects (A_e/A_o) on tides within embayments in the Oligo–Miocene SCS have been estimated and compared to modelled tidal amplitude and convergence effects from 'base-case' tidal model results (Fig. 6). This enables discussion of the differences between theoretical estimations (Eq. 2) and palaeotidal simulations.

For an embayment open at one end (gulf), the simplest period of resonance (T) is a quarter wavelength:

$$T = \frac{4l}{\sqrt{gh}} \quad (3)$$

where *l* = embayment length (m), *g* = gravitational acceleration and *h* = embayment depth (m) (e.g. Allen, 1997). Resonance effects on tides in open-ended embayments/gulfs was determined using Fluidity and simple box models. These were centred on the equator, ranged in size between 0 km and 3000 km wide and 0 to 300 m deep (192 experiments in total) and had a constant bottom drag coefficient of 0.0025 and mesh resolution of *ca* 15 km (Wells, 2008). The model was forced with the M_2, S_2, K_1 and O_1 tidal constituents such that the total boundary tide amplitude was 1 m, the total semidiurnal (i.e. $M_2 + S_2$) and diurnal (i.e. $K_1 + O_1$) constituents had equal tidal magnitudes, and the ratios of semidiurnal and diurnal constituent were equal to the ratio of their equilibrium amplitudes. For each experiment, the tidal range at the head of the embayment was extracted and plotted on a graph of basin width versus depth (Fig. 7). The approximate dimensions of embayments in the Oligo–Miocene SCS have also been plotted to estimate the potential resonance effects on tides within the ancient embayments (Fig. 7).

The relative importance of diurnal (K_1 and O_1) to semidiurnal (M_2 and S_2) tides is quantified using the ratio *F*, where:

$$F = \left(\frac{K_1 + O_1}{M_2 + S_2}\right) \quad (4)$$

If $F < 0.25$, the tide is semi-diurnal, $0.25 < F < 3$, the tide is mixed, and $F > 3$, the tide is diurnal (Open University Course Team, 1999). Double mud and/or carbonaceous drapes, which are an important sedimentological indicator of tides, only form in regions with semi-diurnal tides.

Validation

Tidal amplitude

Astronomical tidal forcing using Fluidity has previously been validated for tidal amplitude in the present-day Baltic, Mediterranean and North seas (Wells et al., 2005a; Wells et al., 2005b; Wells et al., 2007a; Wells et al., 2007b). Tidal modelling using Fluidity has been shown to predict present-day global tidal amplitude to a degree of accuracy that is sedimentologically useful, most notably predicting the following: (i) tidal range to a metre-scale accuracy and identifying microtidal, mesotidal and macrotidal regions (<2 m, 2 to 4 m and >4 m tidal ranges, respectively), which is within the limit of estimating tidal range from the geological record (Wells et al., 2005a); (ii) the position of amphidromic systems; (iii) areas of semidiurnal and diurnal tides; and (iv) regions of tidal amplification due to convergence effects (funnelling and shoaling) (e.g. Wells et al., 2005a; Wells et al., 2007a; Wells et al., 2010a).

The present-day Fluidity tidal models use the GEBCO (General Bathymetric Chart of the Oceans) 2014 bathymetric data, which has a resolution of 1 km (30 arc-seconds) (Weatherall et al., 2015) and an unstructured mesh with maximum resolution of 10 km. The amplitude of the major tidal constituents (M_2, S_2, K_1 and O_1) modelled using Fluidity were compared to the amplitudes calculated using tidal harmonic analysis of sea surface elevation data (Caldwell et al., 2015) from a global

distribution of 423 tidal stations (Fig. 8A to F). The mean root-mean-squared (RMS) error between the modelled and measured data is a comprehensive metric that combines amplitude and phase data and does not include cancellation of positive and negative differences (Cummins and Thupaki, 2018). The relative percentage error between the tidal constituent amplitudes was also calculated. Furthermore, the amplitude of the major tidal consituents modelled using FES2014, a global hydrodynamic tidal model with assimilated data from tidal gauges and satellite altimetry that uses a structured mesh with a *ca* 7 km (1/16°) resolution and 2.9 million nodes (Carrère et al., 2015), were compared to measured data from 162 tidal stations (Fig. 8G to J).

On a global-scale, Fluidity has a slight tendency to underpredict tidal amplitude compared to tidal station data (Caldwell et al., 2015), with the relative error varying between -0.01% (S_2 tide) to -0.23% (O_1 tide) and the RMS amplitude varying between 0.10 m (K_1 and O_1 tide) to 0.37 m (M_2 tide) (Fig. 8C to F). These errors are closely comparable to those between the FES 2014 model and tidal gauge data; FES 2014 has a relative error of between -0.03% (O_1 tide) and -0.14% (S2 tide) and an RMS amplitude between 0.06 m (O_1 tide) and 0.30 m (M_2 tide) (Fig. 8G to J).

The Fluidity tidal model results closely match those of the FES2014 model in shelf areas of the SCS (Fig. 9). This is despite the lower resolution, lack of data assimilation and absence of treatment of internal tide dissipation and load tides, which are important for model accuracy (Egbert et al., 2004). However, Fluidity underpredicts the M_2 tidal amplitude the Philippine Sea by *ca* 33% and the Celebes Sea by *ca* 62%, and underpredicts the K_1 tidal amplitude in the Beibu Gulf by *ca* 30% (Fig. 9; see Fig. 2 for locations). These differences are probably caused by: (i) the coarser mesh resolution of the Fluidity tidal model, which simplifies the bathymetry that affects tidal flow and frictional effects, especially between closely-spaced islands (for example, Philippines); and (ii) the absence of internal drag (Egbert et al., 2004; Wells et al., 2010a).

Bed shear stress

Astronomical tidal forcing using Fluidity has previously been validated for the bed shear stress in the North Sea (Mitchell et al., 2010), which indicated agreement between the following: (i) the pattern and magnitude of maximum bed shear stress of the M_2 tidal constituent modelled using Fluidity and the M_2 and M_4 tidal constituents modelled by Pingree and Griffiths (1979); (ii) the modelled sediment transport vectors of the four main tidal constituents (M_2, S_2, K_1 and O_1) using Fluidity and measured and modelled sand transport vectors (Stride, 1973; Pingree and Griffiths, 1979); and (iii) the modelled distribution of gravel transport of the four main tidal constituents modelled using Fluidity and the observed occurrence of gravel (Graham and Straw, 1992).

In the present-day SCS, the maximum bed shear stress and potential sediment transport modelled using Fluidity have been compared to those modelled using FES 2014, which were calculated based on the modelled tidal current velocity vectors (Eq. 1) (Fig. 10A to D) (Carrère et al., 2015). The difference in sediment grain-size class has also been calculated (Fig. 10E). In general, the pattern of

the modelled maximum bed shear stress in shelf areas of the SCS are similar between Fluidity and FES 2014 but Fluidity overpredicts the maximum bed shear stress (Fig. 10A and C). However, the potential sediment grain-size mobility in shelf areas modelled using Fluidity tends to be the same as, or only one grain size class above, that modelled by FES 2014 (Fig. 10B, D and E). The slight overprediction of sediment grain-size mobility by Fluidity compared to FES 2014 is most likely to be due to the coarser mesh and bathymetry resolution and lack of internal drag, which causes insufficient frictional damping of the tidal energy. These results suggest that Fluidity will be capable of modelling bed shear stress and potential sediment mobility in ancient domains provided that the palaeobathymetric uncertainties are adequately defined (Mitchell et al., 2010).

'Base-case' highstand palaeogeography model results

Model results for 'base-case' highstand palaeobathymetries (Figs 3 and 4) are synthesised for three distinctive sub-regions of the SCS (Fig. 2B): the northern, western and southern SCS (discussed below). Results include tidal range plotted on scales of 0 to 10 m (Fig. 11), 0 to 2 m (Supporting Fig. 2) and 0 to 4 m (Supporting Fig. 3), the 'F-ratio' (Supporting Fig. 4), and the maximum and average bed shear stress, which are plotted as the equivalent grain size that could be entrained if that sediment size was available (Fig. 12 and Supporting Fig. 5).

Northern South China Sea

This area forms a long (*ca* 1500 to 1650 km) but relatively narrow (150 to 300 km), southerly-dipping shelfal area along the eastern margin of the Eurasian continental plate (Figs 3 and 4). Presently this area corresponds to the coastline and drowned shelf of south-west China and east Indochina (Fig. 2). During the Late Oligocene–Early Miocene, this area was closest to the tidal wave entering the SCS from the Pacific Ocean (boundary tide), which moved towards the *ca* SSW through the Luzon Strait and was low mesotidal (Fig. 11A to C). Shoaling effects on shelves in this area amplified the boundary tide, which resulted in mesotidal to macrotidal conditions. In this area tides were capable of transporting up to coarse-grained sand, which had the highest shelf widths (*ca* 200 to 300 km) and boundary tide incidence angles (*ca* >60°) (Fig. 12A to C). In contrast, tides along central southern China were predominantly mesotidal and capable of transporting sand in embayments and narrow (<100 km) straits (Fig. 12A to C). Tidal amplifications along the northern SCS coast may party reflect deflection of the incoming, south-westward propagating tide due to the Coriolis effect. In the Beibu Gulf (location in Fig. 2), complex mesotidal to macrotidal tides enabled transportation of sand–gravel (Fig. 12A to C) due to the interplay of convergence effects, rotation and frictional damping.

During the Middle Miocene, the SCS boundary tide decreased from low mesotidal to microtidal and the prevailing tidal range along open coastlines in the northern SCS decreased from high mesotidal to mesotidal–microtidal (Fig. 11D and E). In shoreline–shelf areas, the potential for tides to transport sand also decreased compared to the Early Miocene (cf. Fig. 12B and C) and gravel transport was only possible within coastal embayments (Fig. 12D and E).

During the Late Miocene, the SCS boundary tide was microtidal and tides along the East Indochina coastline were unable to transport sand (Fig. 11F and G). Along the South China coastline, the shelf width was higher (up to 200 km) and tides were high microtidal and capable of sand transport (Fig. 12F and G). However, tidal range decreased towards the north-east as shelf width decreased (Fig. 11F and G). Funnelling, shoaling and rotation of tides in the Beibu Gulf produced mesotidal tides capable of transporting coarse sand.

Western South China Sea

This area forms the north-eastern margin of the enormous Sunda Platform (Fig. 2), which is presently the largest tropical epicontinental shelf in the world (area *ca* 125,000 km^2) (Hanebuth et al., 2003; Hanebuth et al., 2011) and forms part of the Eurasian continental plate (Figs 3 and 4). Throughout the Neogene this was an emergent and variably elevated area, which formed the south-western head of the SCS gulf and faced the direction of incoming tides from the Pacific Ocean (Figs 3 and 4). The western SCS was characterised by a relatively wide (*ca* 700 to 1500 km north-east/south-west) shelf and a rugose coastline with large, tectonically-related embayments (Fig. 6A and B). During the Late Oligocene, tides in this area were macrotidal and capable of transporting coarse sand to gravel across a large shelf area (Fig. 11A).

During the Late Oligocene–Early Miocene, widespread uplift associated with the initial closure of the proto-SCS and overall marine transgression formed three prominent shallow-marine features (Figs 2 to 4): (i) a wide (>400 km) shelf area; (ii) a large, partially enclosed embayment, the 'East Natuna-Sarawak' (ENS) embayment (Fig. 6B), which had evolved from the merger of two smaller embayments (East Natuna and Sarawak) separated by the recently uplifted (*ca* 21 Ma) Penian High (Fig. 6A); and (iii) initial drowning of a narrow, elongate embayment, the Gulf of Thailand.

During the Early Miocene, tides in the narrow (*ca* 100 km) entrance of the Gulf of Thailand (GOT; equivalent to the West Natuna Basin; Fig. 2) were macrotidal and could transport gravel (Figs 11B, 11C, 12B and 12C). In contrast, tides within the narrow north-west to south-east trending Malay Basin within the GOT were microtidal and only able to transport sand (Figs 11B, 11C, 12B and 12C). Hence, tides within the Early Miocene GOT were dominated by frictional damping rather than by amplification (Figs 6C and 7). In the East Natuna embayment and western ENS embayment, tides were high macrotidal (>10 m) and could transport gravel (Figs 11B, 11C, 12B and 12C), which reflects convergence effects on the dominant K_1 tide (Fig. 6D, 6F and Supporting Fig. 4) and lack of resonance (Fig. 7).

During the Middle Miocene, there was a reduction in tidal range from macrotidal to mesotidal along open coastlines in the western SCS (Fig. 11D and E), which coincided with a decrease in shelf width from *ca* >250 km to *ca* 200 km (Fig. 4D and E). Consequently, the modal sediment grain size transportable by tides decreased from coarse to very fine sand (Fig. 12D and E). Frictional damping of tides in the narrow (<250 km) and shallow (<50 m) entrance to the Middle Miocene GOT

exceeded tidal amplification due to convergence effects (Fig. 6A and C), and the narrow GOT partitioned more tidal energy into the adjacent ENS embayment (Figs 11D, 11E, 12D and 12E). Nonetheless, tides in the GOT were generally mesotidal and capable of transporting coarse sand (Fig. 11D, 11E, 12D and 12E).

Tides in the ENS embayment (Fig. 6B) decreased from macrotidal (5 to 7 m) to high mesotidal–macrotidal (3.5 to 7.0 m) during the Middle Miocene, which was due to a decrease in the boundary tide amplitude and convergence effects (Figs 6F, 11D and 11E). Tidal amplification within the ENS embayment may reflect partial resonance of the M_2 tide (Fig. 7). Within the Middle Miocene western ENS embayment, funnelling and shoaling of tides in the East Natuna embayment (Fig. 6D) produced high macrotidal tides capable of transporting gravel (Figs 11D, 11E, 12D and 12E).

During the early Late Miocene, a wider (*ca* 450 km) and deeper (*ca* 100 m) GOT entrance comprised the West Natuna and Malay basins, which were now connected to the northern GOT; Figs 2A and 4F). This configuration decreased frictional drag and caused constriction and shoaling of the tidal wave, which resulted in macrotidal tides capable of transporting fine gravel (Figs 6B, 11F and 12F). However, tidal range decreased to microtidal in the western GOT due to excess frictional drag (Fig. 11F). Widening and deepening of the GOT decreased convergence effects on tides in the latest Miocene resulting in microtidal–mesotidal conditions (Figs 6C and 11F), but tides could generally transport coarse sand (Fig. 12F). Tidal range highs occur along southern Indochina and eastern Malay Peninsula, which is similar to the present-day (Figs 9 and 11F).

Within the Late Miocene ENS embayment, the East Natuna and Sarawak embayments were no longer separated by the Penian High (Figs 4F to 4G and 6B). Tides in the Late Miocene western ENS embayment decreased from mesotidal to microtidal–mesotidal and were generally unable to transport sand (Figs 11G and 12G). This probably reflects a combination of: (i) more tidal energy entered the GOT; (ii) convergence effects decreased (Fig. 6F); and (iii) further constriction of the tidal waves did not occur within smaller embayments.

Southern South China Sea

This area corresponds to the north-west margin of Borneo and its extension to the north-east into the Palawan area (Fig. 2A). It is geologically more complex than the previous areas, mainly because of south-eastward directed subduction, which was initiated during the Late Oligocene, but continued intermittently throughout the Miocene. The southern SCS margin comprises a broad shelf in the south-west (*ca* 300 km wide; Sarawak Basin and Luconia Platform), but becomes narrower (*ca* 70 to 100 km wide) towards the north-east (Baram Balabac Basin) (Fig. 2). Modelled Late Oligocene to earliest Miocene tides along this margin were generally low macrotidal, apart from in the south-west Sarawak Basin (Fig. 2), due to constriction and shoaling of tides in the Sarawak embayment (Figs 6E and 11A to C). Within the ENS embayment, modelled tides were macrotidal and could transport

coarse sand, which reflect convergence effects on tides in the funnel-shaped embayment (Figs 6D, 8E and 8F).

Prevailing tidal range along southern SCS coastlines decreased from macrotidal to mesotidal during the Middle Miocene, especially in the central ENS embayment where shelf width was highest (200 to 300 km) (Fig. 9A and C). Tides could transport sand along most of north-west Borneo during the early Middle Miocene (Fig. 9B) but could only transport sand in the eastern Sarawak Basin in the late Middle Miocene, despite the potential for convergence effects in the Sarawak embayment (Fig. 6E). Palaeogeographic reconstructions include inferred regions comprising several carbonate build-ups (Figs 3 and 4) in the Luconia Province that correspond to regions of modelled elevated bed shear stress (Fig 12E), which suggests that frictional damping decreased tidal amplitude and velocity prior to entering the Sarawak embayment (Figs 11E and 12E).

In the early Late Miocene, mesotidal tides in the eastern ENS embayment could transport sand in the Luconia Province and along the eastern Sarawak Basin coastline where incoming tides suffered less frictional drag over inferred regions of several shallow carbonate build-ups (Figs 11F and 12F). By the latest Miocene, the embayment was effectively absent and the decreased amplitude of the incoming tide resulted in microtidal tides only capable of sand transport in the Luconia Province (Figs 11G and 12G).

Summary of tidal range and bed shear stress patterns in Oligo–Miocene South China Sea

The base-case palaeotidal model suggests an overall decrease in tidal range and bed shear stress through the Late Oligocene to Miocene in the SCS (Figs 11 to 13 and Supporting Figs 2 to 5). The SCS boundary tide decreased from high microtidal–mesotidal in the Late Oligocene to microtidal in the Middle–Late Miocene (Fig. 13A), which was coincident with a decrease in width of the Luzon Strait from *ca* 1500 km to *ca* 350 km (Fig. 4). The percentage of mesotidal–macrotidal coastline in the SCS decreased from *ca* 100% in the Late Oligocene to *ca* 40% in the latest Miocene; two-thirds of Late Oligocene coastlines were macrotidal but tides were considerably lower by the latest Miocene (Fig. 13D). From the Late Oligocene to Late Miocene, the percentage length of coastline along which sand transport was possible decreased from *ca* 62% to 13% based on the average bed shear stress of modelled tides and from *ca* 94% to 52% based on the maximum bed shear stress of modelled tides (Fig. 13G). However, the modelled present-day tides show a higher average boundary tide, coastline tidal range and bed shear stress (Figs 9 and 10) compared to the late Middle–Late Miocene base-case results (Fig. 13A, D and G). This suggests that more tidal energy is entering the present-day SCS.

Sensitivity analyses

Sensitivity tests were performed on the following 'base-case' palaeotidal modelling results: (i) sensitivity to eustatic sea level uncertainty was investigated using tidal models for palaeobathymetric reconstructions with a 50 m lower sea level (lowstand) (Fig. 14 and Supporting Fig. 1); (ii) sensitivity to the Late Oligocene–Early Miocene positioning of Palawan was investigated using tidal models for palaeogeographic reconstructions where Palawan is submerged (to 10 m) (Fig.

15); and (iii) sensitivity to the palaeobathymetry of the IBM arc was investigated in a Late Miocene (6 Ma) tidal model for a palaeogeographic reconstruction with a submerged (10 m) IBM arc (Fig. 16). For sensitivity tests (ii) and (iii), the submerged depth of 10 m was limited by the methodology of editing the palaeobathymetric meshes and the inability of editing the plate model at the time of simulations. Consequently, only a limited range of palaeogeographic uncertainty has been investigated.

Eustatic sea-level lowstand

During lowstand conditions, the following significant changes to tides occurred: (1) Late Oligocene–Early Miocene western and southern SCS; (2) Early–Late Miocene GOT; and (3) Late Miocene northern SCS (Fig. 12 and Supporting Figs 6 to 11).

(1) Late Oligocene–Early Miocene tides along lowstand coastlines in the western and southern SCS were all macrotidal and generally higher than the highstand tides (Fig. 13D and E). In contrast, the percentage of shorelines along which tides were capable of transporting gravel was lower (50 to 70%) compared to during highstands (80 to 100%) (Fig. 13G and H). Tidal range and bed shear stress maxima occurred due to convergence effects in coastal embayments and/or straits between islands that were smaller or absent during highstands (cf. Figs 11A to C, 12A to C, 14A to D and Supporting Figs 4 to 11).
(2) The size of the Early–Late Miocene GOT decreased during sea-level lowstands (*ca* Figs 3 and 14; see also Supporting Fig. 1) causing increased convergence effects of tides within the ENS embayment (including the East Natuna and Sarawak embayments) during the Early–Middle Miocene (Fig. 14C to F and Supporting Figs 6 to 11). However, tidal range and bed shear stress were relatively higher in the Late Miocene GOT compared to tides in the ENS embayment, and compared to highstand tidal models (*cf*. Figs 11F, 11G, 12F, 12G and 14G to J).
(3) Tides along Late Miocene coastlines in the northern SCS were typically high microtidal–mesotidal during lowstands and unable to transport sand (Fig. 14G to J), whereas highstand tides were microtidal and capable of transporting sand (Figs 11F, 11G, 12F and 12G). This is due to the combination of increased tidal inflow into the SCS forming a higher boundary tide during lowstands (Fig. 13B), which compensates for decreased resonance effects across a narrower shelf (<150 km) (Supporting Fig. 1). However, there was also a potential decrease in both frictional drag and convergence effects on shoreline–shelf tides due to a narrow shelf and straighter shoreline geometry, respectively.

Tides along lowstand SCS coastlines during the Oligo–Miocene show an overall temporal decrease in tidal range and bed shear stress similar to that during sea-level highstand. However, in general, tidal range is higher and tidal bed shear stress is lower. The boundary tide is also generally higher during lowstand (Figs 11, 13 and 14). These changes during lowstands are attributed to: (i) closure of the oceanic connection between the Sea of Japan and Philippine Sea (locations in Fig. 4), which prevented tidal throughflow (e.g. Tsuchi, 1997); and (ii) decreased shelf width, changes to the geometry and bathymetry of coastal embayments, and the formation of several islands, which impacted shoaling, funnelling and resonance effects.

Palaeogeographic positioning of Palawan

Submergence of Palawan to 10 m water depth causes minimal change to tidal dynamics in the SCS (*cf*. Figs 11, 12 and 15; also refer to Supporting Figs 2 to 5 and 12 to 14). The boundary tide is unaffected because Palawan is situated west of the Luzon Strait (Fig. 13C). The percentage length of mesotidal–macrotidal and macrotidal coastline and coastline where sand transport was possible closely matches the base-case palaeotidal model with an emergent Palawan (Fig. 13). Tidal range maxima consistently occur along east Indochina and in the East Natuna embayment (Fig. 15A, C and E). Late Oligocene–Early Miocene tides were capable of transporting coarse sand (Fig. 15B, D and F).

Palaeobathymetry of the Izu–Bonin–Mariana arc

Submergence of the IBM arc to 10 m water depth in the 6 Ma base-case palaeogeography (Fig. 16A and B) results in: (i) a high microtidal SCS boundary tide, which is higher than base-case Messinian boundary tide (Figs 13A, 16C and 16D); and (ii) an increase in the length of mesotidal–macrotidal and macrotidal coastline and coastline along which sand transport was possible compared to the base-case Messinian tidal model (Figs 13 and 16). Therefore, an emergent IBM arc has an important blocking effect on the tide entering the SCS from the Pacific Ocean. Hence, both tidal range and bed shear stress in the Oligo–Miocene SCS were probably higher than the base-case palaeotidal model results.

SEDIMENTARY AND BIOSTRATIGRAPHIC DATA

Methods

The base-case tidal model results have been compared with sedimentological, biostratigraphic and petroleum source-rock data for Oligo–Miocene SCS basins (numbered ‘1’ to ‘8’ in Fig. 17). Referenced datasets contain well-documented facies and/or biostratigraphic data and interpretation of depositional processes and environments. For analyses that only include environmental interpretations, this study has interpreted sedimentary texture and structures based on sedimentary records in adjacent basins and the interpreted depositional environment. Biostratigraphic data suggesting tidal influence are provided by mangrove palynomorphs (pollen) acmes of the genus *Florschuetzia* and/or *Rhizophora*. This is consistent with the distribution of modern mangroves, which are most extensive along tide-dominated, tropical–subtropical shorelines (e.g. Wolanski et al., 1992; Woodroffe et al., 2016).

Sedimentary features indicative of tidal processes at the facies-scale (*ca* millimetre to decimetre) have been extensively documented and include bi-directional cross-lamination/bedding, reactivation surfaces, sigmoidal cross-bedding, mud/carbonaceous drapes and heterolithic bedding (preferably with tidal cyclicity) and ichnofabrics (e.g. De Raaf and Boersma, 1977; Allen, 1981; Allen, 1982; Nio and Yang, 1991; Wells et al., 2005a; Dalrymple and Choi, 2007; MacEachern and Bann, 2008; Martinius and Van den Berg, 2011; Longhitano et al., 2012). However, these features in isolation may be inconclusive evidence of tide-influenced sedimentation (e.g. MacEachern and Bann, 2008; Gugliotta et al., 2016). Palaeo-tidal range analysis requires observations at a range of scales (one to hundreds of kilometres) but can only distinguish microtidal, mesotidal and macrotidal regimes (Wells

et al., 2005a). There is also an inconsistent relationship between present-day tidal range and tidal dominance at the coastline (e.g. Davis and Hayes, 1984). In contrast, tidal bed shear stress quantifies the ability of tides to erode and deposit sediment, with stronger tides having a higher potential to form more tide-influenced morphologies. Validating modelled tidal bed shear stress with sedimentological data is strongly dependent on the grain-size range available during deposition because this controls the type of sedimentary structures preserved (Mitchell et al., 2011). Sediment supply by rivers is the foremost control on grain-size variability in shoreline–shallow marine systems. Tides are unable to affect sedimentary dynamics and preservation if the available sediment was coarser than the maximum sediment calibre that tides could rework. Conversely, tidal bedform size would have increased, or bedform type changed, if the available sediment was finer than the maximum sediment calibre that tides could rework. The comparison between model results and sedimentological and biostratigraphic data is discussed below in relation to the northern, western and southern SCS regions.

Northern South China Sea

Well-documented, Oligo–Miocene palaeoenvironmental analysis is only available for the Pearl River Mouth Basin (basin 1 – Fig. 17). Late Oligocene–Early Miocene deposition is interpreted to have occurred in tide-dominated estuaries and/or deltas (Zheng and Deng, 2012). Modelled tides were mesotidal and capable of transporting coarse sand, which suggests preservation of dune-scale tidal bedforms, provided that the available sand was fine–medium grained or coarser (Fig. 17) (Hjulström, 1939; Harms et al., 1982). Tidal sedimentary structures are not documented in Middle Miocene mixed siliciclastic and carbonate strata despite modelled tides capable of sand transport (Fig. 12). Inferred Late Miocene shelf sand ridges are oriented north-east/south-west and interpreted as lowstand shoreline–deltaic deposits reworked by oceanic currents, waves and tides (Zhuo et al., 2014). This is consistent with the orientation of the modelled tides, which were capable of sand transport (Fig. 12).

Western South China Sea

Mangrove deposits are widespread along the Late Oligocene coastline of the western SCS (southern Indochina and Sunda Platform), particularly in the Nam Con Son Basin in the Early Miocene (Fig. 18) (Shoup et al., 2013). Extensive mangrove deposits also occur along the GOT and southern Indochina coastline in the Middle Miocene but are limited to the Cuu Long Basin and Natuna Arch in the Late Miocene (Fig. 18).

In the Cuu Long Basin (basin 2 – Fig. 17), mangrove pollen acmes in Late Oligocene, late Early Miocene and Middle–Late Miocene strata (Morley et al., 2011; Chung et al., 2015) are consistent with mangrove colonization of a large intertidal area. The latter was subject to macrotidal–mesotidal tides, which were generally capable of transporting sand (Figs 11 and 12). This compares closely with the abundant mangroves in the present-day mesotidal Mekong River delta (Hori, 2000).

In the Nam Con Son Basin (basin 3 – Fig. 17), Late Oligocene strata contain abundant paralic coals and several mangrove pollen acmes (Fig. 18) (Tin and Ty, 1995; Morley et al., 2011; Shoup et al., 2013). Early Miocene strata contain fewer coals and mangrove pollen acmes (Morley et al., 2011) but do include fine–medium grained sandstones interpreted as tidal bars (Fig. 17) (Shoup et al., 2013). There is a significant mangrove pollen acme in the early Middle Miocene (Morley et al., 2011). Tide-influenced and mangrove-influenced deposition throughout the Early–Middle Miocene is consistent with modelled tides capable of reworking coarse sand during this period (Fig. 12B to D). This suggests preservation of dune-scale tidal bedforms in fine–medium grained sandstones (Fig. 17). In contrast, modelled tides in the late Middle–early Late Miocene were generally only capable of transporting silt–very fine sand (Fig. 12E to G), which is consistent with a lack of documented tidal signals in Late Miocene strata (Fig. 17) (e.g. Morley et al., 2011; Shoup et al., 2013).

In the Pattani Basin of the northern GOT (basin 4 – Fig. 17), early Middle Miocene strata contain the primary hydrocarbon source-rocks. These comprise paralic, coal-bearing mudstones containing mangrove pollen, which suggests deposition in a mangrove-vegetated, lower delta plain environment (Jardine, 1997; Lockhart et al., 1997). Modelled tides in the Middle Miocene were high microtidal but capable of transporting coarse sand (Figs 11D, 11E. 12D and 12E), suggesting preservation of dune-scale bedforms in very fine–medium sand (Fig. 17). Middle–Late Miocene strata comprise fine–coarse-grained sandstones deposited primarily in fluvial-dominated, fluvio-deltaic environments, but latest Miocene–Recent strata consist mainly of coals and mudstones with abundant mangrove pollen and subordinate fine–medium-grained sandstones (Jardine, 1997; Lockhart et al., 1997). This is consistent with tides capable of coarse sand transport and an increased intertidal area for mangrove colonization along an expanded GOT coastline (Figs 12, 17 and 18).

In the Malay Basin of the central GOT (basin 5 – Fig. 17), Late Oligocene–Early Miocene and late Middle Miocene strata contain paralic mudstones, laterally extensive coals and abundant mangrove and freshwater flora pollen (Shamsudin and Morley, 2006; Morley et al., 2011). Early–Middle Miocene strata in the West Natuna Basin (southern GOT) also contain paralic mudstones and coals with common mangrove pollen (Morley et al., 2003). This supports mangrove and tropical rainforest colonization of coastal and alluvial plains in the Late Oligocene–Middle Miocene GOT (Fig. 18).

Modelled tides in the Late Oligocene–Middle Miocene GOT were generally microtidal. However, the lower coastal plain of the GOT facilitated extensive mangrove colonization and preservation of tide-influenced sediments by a combination of sheltering from direct wave reworking and increased tidal bed shear stress due to convergence effects in the Early–Middle Miocene (Fig. 12A to E). Mangrove colonization in the GOT has been more limited since the Late Miocene, which is consistent with a decrease in modelled tidal amplitude and strength (Figs 11F, 11G, 12F and 12G), and increased exposure to wave and storm energy.

Southern South China Sea

In the Sarawak Basin (basin 7 – Fig. 17), Early Miocene strata contain abundant mangrove deposits, including *in situ* coals, in association with sandier-upward and thickening-upward, heterolithic to cross-bedded, very-fine grained sandstone units, interpreted as tide-influenced coastal–deltaic successions, and erosional-based, fining-upward, cross-bedded, very-fine grained units, interpreted as fluvio-tidal channel successions (Fig. 19A) (Amir Hassan et al., 2013; Amir Hassan et al., 2016). Mangrove preservation was increased during relative-transgressive phases (e.g. Morley et al., 2003), analogous to mangrove preservation in the Holocene–Present Mekong River delta (Tamura et al., 2009; Li et al., 2012). Fluvial and tidal processes dominated in axial river-mouth positions, where tides were amplified within distributary channels due to convergence effects and where fluvial outflow was augmented by ebb tides. In contrast, mixed-energy, wave-influenced and tide-influenced estuaries and flanking shoreface successions were deposited in areas more susceptible to wave/storm reworking, most notably lateral to active river mouths (Amir Hassan et al., 2013; Collins et al., 2017b). Modelled tides in the Early Miocene of the Sarawak Basin (ENS and Sarawak embayments) were macrotidal and capable of transporting gravel (Figs 11B, 11C, 12B and 12C), which is consistent with common mangrove deposits and tidal cross-bedded, very fine to fine-grained sandstones (Fig. 15).

In the Baram Delta Province, western Baram-Balabac Basin (basin 8 – Fig. 17), Middle–Late Miocene strata are dominated by sandier-upward and thickening-upward units dominated by erosional-based, swaley cross-stratified, very fine-grained sandstones (Fig. 19B). These facies successions are the interpreted result of deposition in mixed-energy, storm-dominated and fluvial-dominated ('storm-flood') delta front and flanking shoreface environments (Collins et al., 2017b). The dominance of storm-dominated, fluvial-influenced deposition in the Middle–Late Miocene Baram Delta Province (BDP) is consistent with modelled tides that are generally mesotidal and unable to transport sand (Figs 11D to G and 12D to G). Tide-dominated deposition and preservation of mangrove carbon-rich mudstones is predominantly confined to structurally-controlled coastal embayments, such as the Berakas Syncline (Collins et al., accepted) and the adjacent offshore areas, such as in the Champion Field (Fig. 19C) (Hadley et al., 2006; Ainsworth et al., 2011). In addition, the preservation potential of tidal sediments was probably relatively low along open coastlines due to storm-reworking but higher in embayments that were sheltered from open shelf waves. This is directly analogous to the modern BDP, where the open coastline Baram delta is wave-dominated and Brunei Bay is both tide-dominated and sheltered open shelf storm waves (Abdul Razak, 2001; Lambiase et al., 2002; Ainsworth et al., 2011; Collins et al., accepted).

DISCUSSION

Utility of palaeotidal modelling for sedimentological analysis

Sedimentological analysis of tidal processes is limited to: (i) determining the relative influence of tidal, wave, storm and fluvial processes on shoreline–shelf deposition and preservation; and (ii) approximately distinguishing microtidal, mesotidal and macrotidal regimes (Wells et al., 2005a). However, numerous sedimentological and ichnological features are inconclusive indicators of tidal

depositional processes. For example, current-rippled heterolithics may indicate fluvial, tidal or mixed fluvial–tidal deposition (Gugliotta et al., 2016; Collins et al., accepted) and mud/carbonaceous drapes are only conclusive tidal indicators if statistical analysis proves an ordered cyclicity of layer thickness and grain size at tidal frequencies (Kvale, 2012). Predicting palaeotidal range from vertical facies successions is compromised by assumptions regarding the preservational completeness of interpreted foreshore and intertidal deposits (Vakarelov et al., 2012; Ainsworth et al., 2015). Similar preservation problems also affect the interpretation of ancient, regional-scale and local-scale geomorphology based on predominantly one-dimensional (for example, stratigraphic logs) and more-limited two-dimensional (for example exposure panels) stratigraphic data (Ainsworth et al., 2011), and comparison with modern analogues (Wells et al., 2005a).

The type and size of bedforms, and hence sedimentary structure, is controlled by current velocity (alternatively expressed as bed shear stress), grain size and water depth (Rubin and McCulloch, 1980; Harms et al., 1982). However, estimates of current velocity (or bed shear stress) from analyses of sedimentary structure, grain size and bedform stability diagrams are limited by: (i) the use of mean flow velocity and mean bed shear stress in bedform stability diagrams because sediment transport and bedform stability will be sensitive to the maximum flow velocity (or bed shear stress); (ii) significant changes in bedform stability fields with changes in water depth (Rubin and McCulloch, 1980; Harms et al., 1982); and (iii) predicting palaeo-water depth from the rock record, which is complex and uncertain (Immenhauser, 2009). Predicting the occurrence of bedforms and sedimentary structures in ancient shoreline–shelf strata based on modelled current velocity and bed shear stress is also challenging because, in the absence of the preserved records, this requires interpretation and assumptions regarding the availability and grain size of sediment during deposition.

Consequently, sedimentological and stratigraphic analyses do not provide definitive quantitative information on ancient tides and validation of palaeotidal simulations. Instead, palaeotidal simulations and sensitivity tests provide an understanding of 'tidal potential' in ancient basins rather than precise quantitative predictions of palaeotidal dynamics (Mitchell et al., 2010; Wells et al., 2010a). The *potential* for tidal influence on shoreline–shelf sedimentation was *relatively high* in the Late Oligocene–Middle Miocene SCS because tidal simulations suggest predominantly mesotidal–macrotidal conditions and widespread potential for sand transport. Conversely, the *potential* for tidal influence on shoreline–shelf sedimentation was *relatively low* in the Late Miocene SCS because tidal simulations suggest predominantly microtidal–low macrotidal conditions and limited potential for sand transport.

Palaeotidal simulations also indicate the potential for tidal amplification within ancient shoreline–shelf embayments. Quantitative estimation of the convergence effects on tides in shoreline–shelf embayments (Eq. 2) (Slingerland, 1986) is limited because the calculation: (i) requires estimation of a single representative value for the width and water depth of the embayment and adjacent shelf regions; (ii) implicitly assumes that tides can freely propagate into the embayment; and (iii) does not

account for frictional damping. Palaeotidal simulations and sensitivity tests can demonstrate the effect of palaeobathymetric uncertainty and include an estimate of frictional damping, which may result in significant differences between calculated and modelled convergence effects on tides in ancient embayments (Fig. 6).

Tectono-physiographic controls on shoreline–shelf tidal processes

Analysis of present-day shoreline–shelf processes (e.g. Harris et al., 2002; Ainsworth et al., 2011; Nyberg and Howell, 2016) and palaeotidal modelling in the Oligo–Miocene of the SCS and other ancient basins (e.g. Mitchell et al., 2010; Wells et al., 2010b) suggests that tides are fundamentally governed by the impact of plate tectonics on three key parameters (Fig. 20A):

1. Coastal and basin position and morphology (for example, width, length, depth, orientation, ocean connection, etc.), which governs regional-scale (hundreds to thousands of kilometres) tidal flow.
2. Tectonic setting, which impacts shelf width and coastal embayment physiography.
3. Relative sea level, which is related to tectonics, climate and drainage basin size (e.g. Nyberg and Howell, 2016) and also impacts shelf width and coastal embayment physiography.

Oligo–Miocene tides in the SCS were strongly influenced by regional-scale (hundreds to thousands of kilometres), plate tectonic changes – the geometry and bathymetry of the IBM arc, Luzon Strait and Sunda Shelf (Fig. 20B) – and local-scale (one to hundreds of kilometres) changes to shelf and coastal embayment physiography (Fig. 20C and D).

Regional (hundreds to thousands of kilometres) controls

An emergent Sunda Shelf created a 'blind' gulf-like geometry that trapped tidal energy within the Oligo–Miocene SCS (Fig. 20B). The wider and deeper ocean connections through the Luzon Strait and north of the IBM arc increased tidal inflow into the SCS (Figs 4, 13 and 20B). These ocean connections became shallower and narrower during the Oligo–Miocene (Fig. 4), resulting in a decrease in tidal range and bed shear stress in the SCS (Fig. 20B).

Sensitivity analyses suggest that regional palaeogeographic uncertainty can exert a significant impact on palaeotidal models in the Oligo–Miocene SCS. First, despite being situated over 1000 km from the Luzon Strait, closure of the oceanic connection into the Sea of Japan (Fig. 2) increased the amplitude of the boundary tides entering the Oligo–Miocene SCS (Figs 13A, 13B and 14). However, prevailing tides in the lowstand SCS remained mostly high mesotidal–macrotidal in the Late Oligocene–Early Miocene, mesotidal in the Middle Miocene, and high microtidal–low mesotidal in the Late Miocene. Second, despite being situated over 1500 km from the Luzon Strait, an emergent IBM arc has a substantial blocking effect on Pacific Ocean tides; when the IBM arc is submerged, coastal tides in the SCS at 6 Ma increase from mostly microtidal to mesotidal.

Local (one to hundreds of kilometres) controls

Analysis of modern tides suggest the relative importance of tides decreases with shelf width perpendicular to the coastline (e.g. Redfield, 1958; Cram, 1979; Howarth, 1982) due to a decrease in the following: (i) tidal prism (Dalrymple, 1992; Yoshida et al., 2007); (ii) tidal resonance potential; and (iii) shoaling effects, especially if sea-bed friction is ignored (e.g. Allen, 1997) (Fig. 18C). However, palaeotidal modelling suggests that this relationship also depends on the following factors:

(1) Frictional damping may exceed tidal amplification due to shoaling of tides across wider shelves (hundreds of kilometres).
(2) Tidal resonance depends on whether tides are semi-diurnal or diurnal. Across straight continental shelves, tides undergo resonance when the shelf width is one-quarter of the tidal wavelength (and for widths 3/4, 5/4, etc.) (Howarth, 1982; Kowalik and Murty, 1993). The wavelengths of the dominant semi-diurnal (M_2) and diurnal (K_1) tides at 100 m depth are 1400 km and 2700 km, respectively (Kowalik and Luick, 2013), which requires very different shelf widths (350 km and 675 km, respectively) to achieve resonance of the M_2 and K_1 tides. In general, tidal range increases with shelf width because the majority (*ca* 70%) of modern shelves are <75 km wide (Nyberg and Howell, 2016) but the correlation between shelf width and tidal range is variable due to changes in the relative amplitude of semi-diurnal to diurnal tides (Howarth, 1982).
(3) The boundary tide incidence angle may also impact tidal resonance. Tides with a lower incidence angle would travel further across the shelf and potentially be closer to resonance (Fig. 20C). This is further impacted by Coriolis rotation, which is related to latitude (Fig. 20C).
(4) Changes to regional-scale tidal flow can supersede the effect of shelf width changes on tidal resonance. For example, despite a decrease in shelf width during lowstands, modelled tidal range along northern SCS coastlines during the Oligo–Miocene was generally higher because the boundary tide had a higher tidal range (for example, Figs 11, 13A, 13B and 14).

Preservation of tide-influenced deposits is favoured by protection from waves and amplification of tides due to convergence and resonance effects in coastal embayments (e.g. Plink-Björklund, 2012). However, palaeotidal modelling in the Oligo–Miocene SCS and other ancient basins (Wells et al., 2007a; Mitchell et al., 2010; Wells et al., 2010b) suggests that tidal amplification in coastal embayments is variable and depends on the balance between amplification due to convergence and/or resonance effects, and damping due to frictional drag. Controls on amplification versus frictional drag include the following: (i) the geometry and bathymetry of the embayment, especially the embayment entrance; (ii) the embayment orientation with respect to the incoming tide; and (iii) the resonance period of the incoming tide (Fig. 20D). Furthermore, tidal range and bed shear stress may be decoupled, as modelled in the Late Miocene GOT (Figs 6A and 10) and the Early Jurassic Laurasian Seaway (e.g. Mitchell et al., 2011), and in the present-day Gulf of Corinth (Piper et al., 1990).

Controls on preservation of shoreline–shelf tidal sediments

Shoreline–shelf stratigraphic successions (e.g. Rossi and Steel, 2016) are a fragmented history of episodic deposition and erosion by competing tidal, wave, storm and fluvial processes (Fig. 21A) (e.g. Dott, 1983; Thorne et al., 1991; Storms, 2003). Preservation of tidal signals depends on the interaction of several processes over a range of timescales (Fig. 1), including the following:

(1) The relative strength and sedimentation rate of tides, fair-weather waves, river floods and storms on a 10^{-3} to 10^{3} year timescale.
(2) The interplay of erosion and deposition during autogenic geomorphic changes (for example, channel/delta lobe switching and mouth bar migration) on a 10^{3} to 10^{5} year timescale.
(3) Long-term (>10^{5} year) patterns of accommodation creation versus destruction and sediment accumulation versus erosion due to allogenic processes.

Formation and preservation of tide-dominated successions requires stronger tidal processes than fluvial and fair-weather wave processes (e.g. Davis and Hayes, 1984; Plink-Björklund, 2012). Spring tides vary on a 10^{-2} to 10^{-1} year timescale whereas daily tides and fair-weather waves occur on a 10^{-6} to 10^{-3} year timescale (Figs 1 and 21B). Therefore, if spring tides have sufficient maximum bed shear stress, they may partially or fully rework the sedimentary record of more frequent but lower magnitude tidal, fluvial and wave processes. Assuming sufficient sediment supply to the coastline, stronger spring tides cause increased reworking and accumulation of thicker beds with higher preservation potential (e.g. Thorne et al., 1991; Wheatcroft and Drake, 2003).

Erosion by higher magnitude-lower frequency river floods, storms and combined storm-river flows ('storm-floods') (Collins et al., 2017b) can prevent preservation of tidal deposits on a thousand-year timescale (Figs 1 and 21B). In coastal–shallow marine systems, low frequency-high magnitude events include storm-generated flows, river-floods and combined storm-river flows ('storm-floods') (e.g. Dott, 1983; Thorne et al., 1991; Miall, 2015; Collins et al., 2017b). In general, the deposits of river floods and storm flow deposits are generally thicker and have a higher preservation potential than tidal deposits, unless the deposits undergo significant post-depositional erosion or bioturbation (Fig. 21B) (*cf*. Dott, 1983). However, tidal deposits will be preserved if they are buried below the level of erosion faster than the repeat time of successive high magnitude-low frequency events. Stronger tides and high sediment availability would increase tidal bed thickness and burial rate, decreasing the transit time through the zone of physical and biogenic reworking, especially if subsidence rates are also relatively high. Characteristic stratigraphic patterns attributed to tidal deposition, including coarsening-upward tidal bars and fining-upward fluvio-tidal channels (Fig. 21A), can be generated by both autogenic and allogenic geomorphic changes over time spans of 10^{1} to 10^{3} and 10^{3} to 10^{6} years, respectively (Fig. 1).

On longer timescales (>10^{3} years), tidal deposits are only preserved if accommodation creation and sedimentation favours continued burial and lithification, and erosion is avoided. In general, higher rates of accommodation creation favour formation of thicker stratigraphic successions and higher burial rates, resulting in increased preservation potential (Ainsworth et al., 2017). Large-scale (tens to thousands of kilometres) changes in accommodation and sedimentation patterns in depositional systems are caused by eustatic sea level variations, principally driven by climate cycles at Milankovitch frequencies (10^{4} to 10^{6} year), and tectonic processes (10^{6} to 10^{7} years) (Fig. 1).

CONCLUSIONS

1. Seven highstand palaeobathymetric reconstructions of the Oligo–Miocene SCS region indicate rapid and substantial changes to regional-scale (hundreds to thousands of kilometres) physiography and local-scale (one to hundreds of kilometres) shelf physiography and coastline rugosity. Palaeotidal modelling using an astronomically-forced and global tidal model (Fluidity) at a maximum 10 km resolution, suggests that in the Late Oligocene–early Middle Miocene (*ca* 26 to 15 Ma) SCS, >80% of coastline spring tides were mesotidal–macrotidal (>2 m), >30% were macrotidal (>4 m) and sand transport was possible along 80% of the coastline. Variations in regional boundary tide dynamics, controlled by the positioning and bathymetry of the Philippines and IBM arc, was the foremost control on shelf tides and often outweighed changes in tidal resonance potential related to shelf width. In shoreline–shelf embayments and straits, tidal amplification due to convergence effects (funnelling and shoaling) versus damping due to frictional drag was variable and controlled by embayment physiography (especially the entrance), orientation and the resonance period of the incoming tide.
2. During sea-level lowstands (*ca* 50 m), a shutdown of tidal throughflow into the Sea of Japan increased tidal inflow into the SCS, which superseded a decrease in tidal resonance across narrower shelves. Changes in coastal embayment physiography and formation of islands controlled the re-distribution of tidal range and bed shear stress maxima.
3. An emergent IBM arc had a significant blocking effect on Pacific Ocean tides entering the Oligo–Miocene SCS. When the IBM arc is submerged to a water depth of 10 m in the latest Miocene, increased tidal inflow caused an average *ca* 30% increase in the percentage length of mesotidal–macrotidal and macrotidal coastline and coastline along which tides could transport sand.
4. Oligo–Miocene sedimentological and biostratigraphic data in SCS basins compare favourably with palaeotidal model results, including the distribution and sedimentary fabric of tide-influenced, shoreline–shelf successions and mangrove sediments. However, the preservation potential of Early–Late Miocene, tide-influenced sediments was higher in the wave-protected embayments (for example, the Gulf of Thailand) compared with the open coastlines such as along north-west Borneo, where ancient successions deposited outside of shoreline–shelf embayments were predominantly storm-wave-reworked. Higher magnitude-lower frequency events, such as 100 to 1000 year storms and river floods, have a higher preservation potential on geological ($\geq 10^4$ year) timescales.

ACKNOWLEDGEMENTS

This work was funded by a NERC PhD scholarship (DSC). Fieldwork was supported by Shell International Exploration and Production (DSC and HDJ). We also acknowledge the support of Getech (DSC, AA and PAA) as well as Imperial College's Grantham Institute (MDP), and High Performance Computing Service. We also thank M. van Cappelle and C.D. Dean for fieldwork assistance and many other geoscientists for stimulating discussions during field excursions to north-west Borneo: G.J. Hampson, D.M. Hodgson, B.K. Levell and R.B. Ainsworth are thanked for valuable comments and discussion.

FIGURE CAPTIONS

Fig. 1. The repeat time, instantaneous sedimentation rates and thickness of deposits associated with sedimentary processes that control deposition, accommodation space creation and erosion of sediment during burial and lithification (modified from Miall, 2015).

Fig. 2. Location map of study area. (A) Topographic and bathymetric map of the South China Sea (SCS) showing simplified plate tectonic framework, structural elements, and major sedimentary basins (pink lines and abbreviations). Labelled basins are (anticlockwise): PRMB = Pearl River Mouth Basin; BB = Beibuwan Basin; QB = Quiongdongnan Basin; PKB = Phu Khanh Basin; CL = Cuu Long Basin; NCSB = Nam Con Son Basin; PAB = Pattani Basin; MB = Malay Basin; PB = Penyu Basin; WNB = West Natuna Basin; ENB = East Natuna Basin; LP = Luconia Province; SB = Sarawak Basin; BBB = Baram-Balabac Basin. Additional labels (alphabetical order): ASRRF = Ailao Shan–Red River Fault; BG = Beibu Gulf; BPT = north-west Borneo–Palawan Trough; DG = Dangerous Grounds; GOT = Gulf of Thailand; LS = Luzon Strait; MP = Malay Peninsula; MS = Malacca Strait; NA = Natuna Arch; Pal. = Palawan; PS = Philippine Sea; RB = Reed Bank Block; SS = Sunda Shelf. (B) Informal subdivision of the SCS into northern, southern and western regions.

Fig. 3. Gross depositional environmental reconstructions for the Late Oligocene–Late Miocene in Southeast Asia based on sea-level highstand for eight time-slices: (A) 26 Ma (Chattian); (B) 21 Ma (Aquitanian); (C) 18 Ma (Burdigalian); (D) 15 Ma (Langhian); (E) 12 Ma (Serravallian); (F) 11 Ma (Tortonian); (G) 6 Ma (Messinian). Alternative gross depositional environmental reconstructions include a submerged Palawan: (H) 26 Ma (Chattian); (I) 21 Ma (Aquitanian); (J) 18 Ma (Burdigalian).

Fig. 4. Palaeobathymetric reconstructions for the Late Oligocene–Late Miocene and present-day bathymetry in Southeast Asia based on sea-level highstand for eight time-slices: (A) 26 Ma (Chattian); (B) 21 Ma (Aquitanian); (C) 18 Ma (Burdigalian); (D) 15 Ma (Langhian); (E) 12 Ma (Serravallian); (F) 11 Ma (Tortonian); (G) 6 Ma (Messinian); and (H) Present-day. See Fig. 3 for the gross depositional environment reconstructions for Fig. 4A to G.

Fig. 5. General stratigraphic columns from 14 representative basins located around the periphery of the South China Sea (SCS; see Fig. 2 for basin locations). Formations are shaded for interpreted gross depositional environment (see colour legend). Palaeogeographic reconstruction and tidal model time-slices are labelled in the chronostratigraphic column. Basin names and references: N PRMB = North Pearl River Mouth Basin (Chen et al., 1994; Zhu et al., 2009); BB = Beibuwan Basin (Li et al., 2008); QB = Quiongdongnan Basin (Huang et al., 2003; Zhu et al., 2009); PKB = Phu Khanh Basin (Lee and Watkins, 1998; Fyhn et al., 2009); NCS = Nam Con Son Basin (Matthews et al., 1997; Lee et al.,

2001; Morley et al., 2011); CL = Cuu Long Basin (Lee et al., 2001); ENB = East Natuna Basin (Darman and Sidi, 2000); WNB = West Natuna Basin (Morley et al., 2011); PB = Penyu Basin (Madon and Anuar, 1999); MB = Malay Basin (Madon et al., 1999; Morley et al., 2011); LP = Luconia Province (Madon, 1999; Mohammad Yamin and Abolins, 1999); NE SB = North-east Sarawak Basin (Mazlan, 1999); SW BBB = South-west Baram-Balabac Basin (Sandal, 1996; Hutchison, 2005); NE BBB = North-east Baram-Balabac Basin (Sandal, 1996; Hutchison, 2005). Formation names (in approximate relative age order from youngest to oldest for each basin) are given in the Supporting Information and in Fig. 17.

Fig. 6. Comparison between calculated and modelled convergence effects (funnelling and shoaling) in Oligo–Miocene embayments in the part of the western and southern South China Sea (SCS; see Fig. 2B for approximate location). (A) and (B) Location of embayments in the 21 Ma (A) and 12 Ma (B) time slices (see Fig. 3 for other time slices). (C) Early–Late Miocene Gulf of Thailand (GOT). (D) Early–Middle Miocene East Natuna (EN) embayment. (E) Early–Middle Miocene Sarawak (S) embayment. (F) Middle–Late Miocene East Natuna-Sarawak (ENS) embayment.

Fig. 7. Graph of increase in tidal range of the semidiurnal (M_2 and S_2) and diurnal (K_1 and O_1) tidal constituents due to resonance in basins of various dimensions. Approximate dimensions of Gulf of Thailand (GOT), East Natuna (EN), East Natuna-Sarawak (ENS) and Sarawak (S) embayments are plotted using open or black-filled symbols. Open symbols are for quarter-wave resonating embayments open at one end and black-filled symbols are for half-wave resonating 'enclosed' water bodies (in this case the GOT embayment). The time-slice age is given as a subscript for each embayment symbol.

Fig. 8. Validation of Fluidity and FES2014 model (Carrère et al., 2015) tidal amplitude simulations to tidal station data. (A) Number (n) and position of global dataset of tidal stations used for the comparisons. Tidal stations used for the FES2014 comparison (red; n = 162) were also used for the Fluidity comparison (yellow; n = 423). (B) Position of tidal stations used for the comparisons in the SCS, with the informal sub-regions labelled. (C) to (J) Plots of tidal amplitude calculated based on measured sea surface elevation data from tidal stations versus modelled tidal amplitude for the K_1 (A) and (E), M_2 (B) and (F), O_1 (C) and (G) and S_2 (D) and (H) tidal constituents using Fluidity (A) to (D) and FES2014 (E) to (H). The mean root-mean-squared (RMS) error, relative percentage error and number of tidal gauge stations (n) used for comparison are stated.

Fig. 9. Comparison of M_2 and K_1 tide amplitudes (0 to 1 m) in the present-day South China Sea (SCS) modelled using Fluidity (A) and (B) and FES2014 (C) and (D). Abbreviations are listed in Fig. 2.

Fig. 10. Comparison of modelled maximum tidal bed shear stress and potential grain-size mobility using Fluidity and FES2014 (Carrère et al., 2015) in the present-day SCS. (A) Maximum bed shear stress modelled using Fluidity. (B) Potential grain-size mobility modelled using Fluidity. (C) Maximum bed shear stress modelled using FES2014. (D) Potential grain-size mobility modelled using FES2014. (E) Grain-size class difference in the potential sediment mobility modelled by Fluidity (Fig. 10B) and FES2014 (Fig. 10D). Grain-size abbreviations: vfs = very fine sand; fs = fine sand; ms = medium sand; cs = coarse sand; vcs = very coarse sand; fg = fine gravel; cg = coarse gravel. Other abbreviations are listed in Fig. 2.

Fig. 11. Base-case tidal model results for tidal range for seven timeslices in the Oligo–Miocene in Southeast Asia: (A) 26 Ma (Chattian); (B) 21 Ma (Aquitanian); (C) 18 Ma (Burdigalian); (D) 15 Ma (Langhian); (E) 12 Ma (Serravallian); (F) 11 Ma (Tortonian); (G) 6 Ma (Messinian). The thicker black line is the reconstructed present-day coastline. The 200 m palaeobathymetric contour (pink) is the approximate palaeo-shelf edge. Refer to Supporting Figs 2 to 4 for replotted base-case tidal range (0 to 2 m and 0 to 4 m) and F-ratio model results for all time-slices.

Fig. 12. Base-case tidal model results for maximum tidal bed shear stress, plotted as the maximum sediment calibre that could be entrained if available, for seven timeslices in the Oligo–Miocene in Southeast Asia: (A) 26 Ma (Chattian); (B) 21 Ma (Aquitanian); (C) 18 Ma (Burdigalian); (D) 15 Ma (Langhian); (E) 12 Ma (Serravallian); (F) 11 Ma (Tortonian); (G) 6 Ma (Messinian). Refer to Fig. 11 for legend details and Supporting Fig. 5 for potential sediment mobility based on modelled average tidal bed shear stress for all time-slices. Grain-size abbreviations: vfs = very fine sand; fs = fine sand; ms = medium sand; cs = coarse sand; vcs = very coarse sand; fg = fine gravel; cg = coarse gravel.

Fig. 13. Summary of tidal model results for Oligo–Present-day SCS base-case (highstand) simulations (A), (D) and (G) and the following sensitivity analyses: (A), (C) and (D) submerged IBM arc; (B), (E) and (H) 50 m sea level lowstand; and (C), (F) and (I) submerged Palawan. Results shown are: (A) to (C) boundary tide tidal range (maximum, median and minimum); (D) to (F) the percentage length of mesotidal–macrotidal (>2 m) and macrotidal (>4 m) coastline; (G) to (I) the percentage length of coastline along which sand transport was possible by average and maximum strength (bed shear stress, BSS) tides. The dashed vertical line is the Oligocene–Miocene boundary (*ca* 23 Ma). Refer to Figs 8 to 10 and Supporting Figs 2 to 5 for base-case model results, Fig. 12 and Supporting Figs 6 to 11 for 50 m sea level lowstand model results, Fig. 13 and Supporting Figs 12 to 14 for submerged Palawan model results, and Fig. 14 and Supporting Fig. 15 for submerged IBM arc results.

Fig. 14. Tidal model results for 50 m sea level lowstand showing tidal range (A), (C), (E), (G) and (I) and maximum tidal bed shear stress, plotted as the maximum sediment calibre entrained (B), (D), (F), (H) and (J), for Late Oligocene–Late Miocene palaeobathymetric reconstructions: (A) and (B) 26 Ma (Chattian); (C) and (D) 21 Ma (Aquitanian); (E) and (F) 15 Ma (Langhian); (G) and (H) 11 Ma (Tortonian); and (I) and (J) 6 Ma (Messinian). Refer to Supporting Figs 6 to 11 for remaining time-slice model results (18 Ma and 12 Ma), replotted tidal range (0 to 2 m and 0 to 4 m), F-ratio and average tidal bed shear stress model results for all time-slices. Grain-size abbreviations: vfs = very fine sand; fs = fine sand; ms = medium sand; cs = coarse sand; vcs = very coarse sand; fg = fine gravel; cg = coarse gravel.

Fig. 15. Tidal model results for tidal range (A), (D) and (G) and maximum tidal bed shear stress, plotted as the maximum sediment calibre entrained (B), (E) and (H) for Late Oligocene–Early Miocene palaeobathymetric reconstructions with Palawan submerged to *ca* 10 m water depth (see Fig. 2 for location). (A) and (B) 26 Ma (Chattian); (C) and (D) 21 Ma (Aquitanian); and (E) and (F) 18 Ma (Burdigalian). Refer to Supporting Figs 12 to 14 for replotted tidal range (0 to 2 m and 0 to 4 m), F-ratio and average tidal bed shear stress model results. Grain-size abbreviations: vfs = very fine sand; fs = fine sand; ms = medium sand; cs = coarse sand; vcs = very coarse sand; fg = fine gravel; cg = coarse gravel.

Fig. 16. Tidal model results for Late Miocene (6 Ma) palaeobathymetric reconstruction with a submerged IBM arc showing: (A) palaeobathymetric interpretation (*cf.* Fig. 3G); (B) tidal range (*ca* Fig. 10C); and (C) maximum tidal bed shear stress, plotted as the maximum sediment calibre entrained (*ca* Fig. 10D). Refer to Supporting Fig. 15 for replotted tidal range (0 to 2 m and 0 to 4 m), average tidal bed shear stress and F-ratio model results. Grain-size abbreviations: vfs = very fine sand; fs = fine sand; ms = medium sand; cs = coarse sand; vcs = very coarse sand; fg = fine gravel; cg = coarse gravel.

Fig. 17. Comparison of sedimentological and biostratigraphic rock data, mainly from petroleum exploration wells, preserving evidence of tide-influenced deposition and base-case tidal model results in the SCS basins. Rock data include grain size, tide-generated cross-lamination (ripples) and/or cross-bedding (mainly in siltstone–sandstone facies), mangrove pollen acmes (mainly in mudstones and/or coals), and the occurrence of paralic, mangrove-influenced coals and source-rocks (coals or carbonaceous mudstones). Studied formations and data sources for each basin are: (1) Upper Zhuhai (Zh) Formation, Pearl River Mouth Basin (Zheng and Deng, 2012); (2) Bach Ho (BH) and Con Son (CS) formations, Cuu Long Basin (Morley et al., 2011); (3) Dua (Du), Thong (Th) and Mang Cau (MC) formations, Nam Con Son Basin (Tin and Ty, 1995; Morley et al., 2011); (4) Sequences II–IV, Pattani Basin (Jardine, 1997; Lockhart et al., 1997); (5) Groups L–J and E, Malay Basin (Morley et al., 2011); (6) Arang (Ar) Formation, West Natuna Basin (Morley et al., 2011); (7) Nyalau (Ny) Formation, Balingian Province, Sarawak Basin (Amir Hassan et al., 2013; Amir Hassan et al., 2016); (8) Lambir (L) and Belait (B) formations, Baram Delta Province, Baram-Balabac Basin (Lambiase et al., 2003; Collins et al.).

Fig. 18. Palaeogeographic reconstructions of depositional coastlines in the western South China Sea (SCS) during the Oligo–Miocene: (A) 26 Ma (Chattian); (B) 21 Ma (Aquitanian); (C) 18 Ma (Burdigalian); (D) 15 Ma (Langhian); and (E) 6 Ma (Messinian). Maps are modified from Shoup et al. (2013). Note that the palaeobathymetry of the 15 Ma time-slice (D) was simplified for tidal modelling (*cf.* Figs 3 and 4). Pink lines outline sedimentary basins (refer to Fig. 17 for legend to numbers). NA = Natuna Arch.

Fig. 19. Examples of coastal–shallow marine stratigraphic preservation in the southern South China Sea (SCS) during the Oligo–Miocene. (A) Tide-dominated facies associations in the offshore Balingian Province, Sarawak Basin, include (pink numbers) mangrove facies in abandoned fluvial-tidal channels '1' and associated with tidal bars/delta front '2' (after Amir Hassan et al., 2016). (B) The Middle–Late Miocene Belait Formation, onshore western BBB (Berakas Syncline) is dominated by wave-dominated, fluvial-influenced (storm-flood-dominated) facies successions with subordinate preservation of tide-influenced facies associations (Collins et al., 2017b; Collins et al.). (C) Simplified cross-section of Late Miocene strata in Champion Field, offshore Baram Delta Province, western Baram-Balabac Basin (BBB). Tide-dominated mouth bars, channels and restricted bay facies form distinct stratigraphic intervals from the dominant wave-dominated shoreface/delta front successions (after Ainsworth et al., 2011).

Fig. 20. (A) Interplay of factors influencing tidal processes on a regional-scale (hundreds to thousands of kilometres) boundary tide dynamics and a relatively local (one to hundreds of kilometres), shelf and embayment tides (Nyberg and Howell, 2016). (B) The dynamics of the boundary tide entering the South China Sea (SCS) during the Oligo–Miocene was controlled by relative inflow past the Izu–Bonin–Mariana (IBM) arc and through the Luzon Strait, throughflow in the Philippines Sea (PS) and outflow from the SCS, which was significantly blocked by an emergent Sunda Shelf (SS). (C) Influence of shelf width on resonance versus frictional drag of tides. Tides travelling directly perpendicular to straight shelves will resonate when shelf width approaches one-quarter the tide wavelength (λ), but shelf geometry and the incident angle (θ) and rotation of tides (determined by latitude and the Coriolis force) will vary the distance tides travel across the shelf (dashed arrow) and the resonance potential. (D) The amount of tidal inflow, amplification due to convergence effects, and frictional damping of tides in coastal embayments is controlled by the geometry (for example, sinuosity/rugosity) of embayment, size and depth (physiography) of the embayment entrance, and the orientation of the embayment entrance relative to the incident angle of the incoming tide.

Fig. 21. (A) Schematic logs illustrating the differences between the preserved sedimentary records of tide-dominated, wave-dominated, river-dominated and mixed-energy coastal–deltaic to shallow-marine systems (after Rossi and Steel, 2016). Shading represents process dominance or mix. The preserved 'time' record for each log emphasises the importance of gaps and deposition during higher magnitude-lower frequency events (pink) compared to lower magnitude-higher frequency background sedimentation (light green) (cf. Dott, 1983). Refer to Fig. 19 for sedimentological legend. Grain-size abbreviations: M = mud; vf = very fine sand; f = fine sand; m = medium sand; c = coarse sand; vc = very coarse sand; g = gravel. (B) Ternary phase diagram plot illustrating the differences in preservation potential of deposits of tides (daily and spring), fair-weather waves, river floods (seasonal to 100 year) and storm flows (seasonal to 1000 year). Preservation potential increases with increasing thickness of sediment deposited per event, decreasing frequency (inverse of the repeat time) and reworking during the event.

REFERENCES

Abdul Razak, D. (2001) *Brunei Bay, Northwest Borneo: Depositional System*, University of Aberdeen, 529 pp.

Ager, D.V. (1993) *The New Catastrophism*. Cambridge University Press, Cambridge, UK, 251 pp.

Ainsworth, R.B., Vakarelov, B.K., Lee, C., MacEachern, J.A., Montgomery, A.E., Ricci, L.P. and Dashtgard, S.E. (2015) Architecture and evolution of a regressive, tide-influenced marginal marine succession, Drumheller, Alberta, Canada. *J. Sed. Res.*, **85,** 596-625.

Ainsworth, R.B., Vakarelov, B.K., MacEachern, J.A., Rarity, F., Lane, T.I. and Nanson, R.A. (2017) Anatomy of a Shoreline Regression: Implications for the high-resolution stratigraphic architecture of deltas. *J. Sed. Res.*, **87,** 425-459.

Ainsworth, R.B., Vakarelov, B.K. and Nanson, R.A. (2011) Dynamic spatial and temporal prediction of changes in depositional processes on clastic shorelines: Toward improved subsurface uncertainty reduction and management. *Am. Assoc. Pet. Geol. Bull.*, **95,** 267-297.

Allen, J.R.L. (1981) Palaeotidal speeds and ranges estimated from cross-bedding sets with mud drapes. *Nature*, **293,** 394-396.

Allen, J.R.L. (1982) Mud drapes in sand-wave deposits: a physical model with application to the Folkestone Beds (early Cretaceous, southeast England). *Phil. Trans. R. Soc. A*, **306,** 291-345.

Allen, P.A. (1997) *Earth Surface Processes*. Blackwell Scientific Publications, Oxford, U.K., 404 pp.

Almasco, J.N., Rodolfo, K., Fuller, M. and Frost, G. (2000) Paleomagnetism of Palawan, Philippines. *J. Asian Earth Sci.*, **18,** 369-389.

Amir Hassan, M.H., Johnson, H.D., Allison, P.A. and Abdullah, W.H. (2013) Sedimentology and stratigraphic development of the upper Nyalau Formation (Early Miocene), Sarawak, Malaysia: A mixed wave- and tide-influenced coastal system. *J. Asian Earth Sci.*, **76,** 301-311.

Amir Hassan, M.H., Johnson, H.D., Allison, P.A. and Abdullah, W.H. (2016) Sedimentology and stratigraphic architecture of a Miocene retrogradational, tide-dominated delta system: Balingian Province, offshore Sarawak, Malaysia. In: *Sedimentology of Paralic Reservoirs: Recent Advances* (Eds G.J. Hampson, A.D. Reynolds, B. Kostic and M.R. Wells), *Special Publications*, **444**, pp. SP444.12, 36 p. Geological Society of London, London, UK.

Aurelio, M.A., Forbes, M.T., Taguibao, K.J.L., Savella, R.B., Bacud, J.A., Franke, D., Pubellier, M., Savva, D., Meresse, F. and Steuer, S. (2014) Middle to Late Cenozoic tectonic events in south and central Palawan (Philippines) and their implications to the evolution of the south-eastern margin of South China Sea: Evidence from onshore structural and offshore seismic data. *Mar. Pet. Geol.*, **58,**

658-673.
Avdis, A., Candy, A.S., Hill, J., Kramer, S.C. and Piggott, M.D. (2018) Efficient unstructured mesh generation for marine renewable energy applications. *Renew. Energy*, **116,** 842-856.
Balaguru, A. and Hall, R. (2008) Tectonic Evolution and Sedimentation of Sabah, North Borneo, Malaysia. In: *Search and Discovery Article #30084, AAPG International Conference and Exhibition*, Cape Town, South Africa.
Barckhausen, U., Engels, M., Franke, D., Ladage, S. and Pubellier, M. (2014) Evolution of the South China Sea: Revised ages for breakup and seafloor spreading. *Mar. Pet. Geol.*, **58,** 599-611.
Barckhausen, U. and Roeser, H.A. (2004) Seafloor spreading anomalies in the South China Sea revisited. In: *Continent-Ocean Interactions Within East Asian Marginal Seas* (Eds P. Clift, W. Kuhnt, P. Wang and D. Hayes), *Geophysical Monograph Series*, pp. 121-125. AGU, Washington, DC.
Barrell, J. (1917) Rhythms and the measurements of geologic time. *Geol. Soc. Am. Bull.*, **28,** 745-904.
Briais, A., Patriat, P. and Tapponnier, P. (1993) Updated interpretation of magnetic anomalies and seafloor spreading stages in the south China Sea: Implications for the Tertiary tectonics of Southeast Asia. *J. Geophys. Res.*, **98,** 6299-6328.
Buatois, L.A., Santiago, N., Herrera, M., Plink-Björklund, P., Steel, R.J., Espin, M. and Parra, K. (2012) Sedimentological and ichnological signatures of changes in wave, river and tidal influence along a Neogene tropical deltaic shoreline. *Sedimentology*, **59,** 1568-1612.
Caldwell, P., Merrfield, M. and Thompson, P. (2015) Sea level measured by tide gauges from global oceans–the Joint Archive for Sea Level holdings (NCEI Accession 0019568), Version 5.5. National Oceanographic Data Center, NOAA. Dataset. 2015.
Carrère, L., Lyard, F., Cancet, M. and Guillot, A. (2015) FES 2014, a new tidal model on the global ocean with enhanced accuracy in shallow seas and in the Arctic regio. In: *EGU General Assembly 2015*, Vienna, Austria.
Chen, J., Xu, S. and Sang, J. (1994) The depositional characteristics and oil potential of paleo Pearl River delta systems in the Pearl River Mouth basin, South China Sea. *Tectonophysics*, **235,** 1-11.
Chen, S., Steel, R.J., Dixon, J.F. and Osman, A. (2014) Facies and architecture of a tide-dominated segment of the Late Pliocene Orinoco Delta (Morne L'Enfer Formation) SW Trinidad. *Mar. Pet. Geol.*, **57,** 208-232.
Chung, N.H., Quang, C.D. and Tham, N.T. (2015) A Review of Tertiary Palynomorph Assemblage in Cuu Long Basin: Case Study of Palynomorphs in Miocene–Oligocene Sediments. *IJSBAR*, **24,** 103-111.
Coleman, J.M. and Wright, L.D. (1975) Modern river deltas: variability of processes and sand bodies. In: *Deltas: Models for Exploration* (Ed M.L. Broussard), pp. 99-149. Houston Geological Society, Houston, Texas.
Collins, D.S., Avdis, A., Allison, P.A., Johnson, H.D., Hill, J., Piggott, M.D., Hassan, M.H.A. and Damit, A.R. (2017a) Tidal dynamics and mangrove carbon sequestration during the Oligo–Miocene in the South China Sea. *Nat. Commun.*, **8,** 15698.
Collins, D.S., Johnson, H.D., Allison, P.A. and Damit, A.R. (accepted) Mixed Process, Humid-Tropical, Shoreline–Shelf Deposition: Middle Miocene–Modern Baram Delta Province, North-West Borneo. *J. Sed. Res.*
Collins, D.S., Johnson, H.D., Allison, P.A., Guilpain, P. and Damit, A.R. (2017b) Coupled 'storm-flood' depositional model: Application to the Miocene–Modern Baram Delta Province, north-west Borneo. *Sedimentology*, **64,** 1203–1235.
Cram, J.M. (1979) The influence of continental shelf width on tidal range: paleoceanographic implications. *J. Geol.*, **87,** 441-447.
Cummins, P.F. and Thupaki, P. (2018) A note on evaluating model tidal currents against observations. *Cont. Shelf Res.*, **152,** 35-37.
Cushman-Roisin, B. and Beckers, J.-M. (2011) *Introduction to Geophysical Fluid Dynamics: Physical and Numerical Aspects*. Academic Press, Cambridge, MA, 875 pp.
Dalrymple, R.W. (1992) Tidal depositional systems. In: *Facies Models: Response to Sea Level Change* (Eds R.G. Walker and N.P. James), pp. 195-218. Geological Association of Canada, St. John's,

Newfoundland.
Dalrymple, R.W. and Choi, K. (2007) Morphologic and facies trends through the fluvial–marine transition in tide-dominated depositional systems: A schematic framework for environmental and sequence-stratigraphic interpretation. *Earth-Science Reviews*, **81,** 135-174.
Darman, H. and Sidi, F.H. (2000) *An outline of the geology of Indonesia*. Indonesian Association of Geologists, Jakarta, 192 pp.
Davis, R.A. and Dalrymple, R.W. (2011) *Principles of Tidal Sedimentology*. Springer, New York, 621 pp.
Davis, R.A. and Hayes, M.O. (1984) What is a wave-dominated coast? *Mar. Geol.*, **60,** 313-329.
De Raaf, J.F.M. and Boersma, J.R. (1977) Tidal deposits and their sedimentary structures (seven examples from Western Europe). *Geol. Mijnbouw*, **50,** 479-504.
Dott, R.H. (1983) Episodic Sedimentation—How Normal Is Average? How Rare Is Rare? Does It Matter? *J. Sediment. Petrol.*, **53,** 5-23.
Doust, H. and Sumner, H.S. (2007) Petroleum systems in rift basins—a collective approach in Southeast Asian basins. *Pet. Geosci.*, **13,** 127-144.
Egbert, G.D., Ray, R.D. and Bills, B.G. (2004) Numerical modeling of the global semidiurnal tide in the present day and in the last glacial maximum. *Journal of Geophysical Research: Oceans*, **109**.
Foreman, M.G.G. (1979) *Manual for Tidal Heights Analysis and Prediction*. Institute of Ocean Sciences, Patricia Bay, Sidney, B.C., 58 pp.
Franke, D., Barckhausen, U., Heyde, I., Tingay, M. and Ramli, N. (2008) Seismic images of a collision zone offshore NW Sabah/Borneo. *Mar. Pet. Geol.*, **25,** 606-624.
Fyhn, M.B.W., Nielsen, L.H., Boldreel, L.O., Thang, L.D., Bojesen-Koefoed, J., Petersen, H.I., Huyen, N.T., Duc, N.A., Dau, N.T., Mathiesen, A., Reid, I., Huong, D.T., Tuan, H.A., Hien, L.V., Nytoft, H.P. and Abatzis, I. (2009) Geological evolution, regional perspectives and hydrocarbon potential of the northwest Phu Khanh Basin, offshore Central Vietnam. *Mar. Pet. Geol.*, **26,** 1-24.
Gaina, C. and Müller, D. (2007) Cenozoic tectonic and depth/age evolution of the Indonesian gateway and associated back-arc basins. *Earth-Science Reviews*, **83,** 177-203.
Galloway, W.E. (1975) Process framework for describing the morphologic and stratigraphic evolution of deltaic depositional systems. In: *Deltas: Models for Exploration* (Ed M.L. Broussard), pp. 87-98. Houston Geological Society, Houston, Texas.
Geuzaine, C. and Remacle, J.F. (2009) Gmsh: A 3-D finite element mesh generator with built-in pre- and post-processing facilities. *Int J Numer Meth Eng*, **79,** 1309-1331.
Graham, C.G. and Straw, A. (1992) Quaternary. In: *Atlas of Palaeogeography and Lithofacies* (Eds J.C.W. Cope, J.K. Ingham and P.F. Rawson), **13**, pp. 149–153. Geological Society London Memoir.
Gugliotta, M., Kurcinka, C.E., Dalrymple, R.W., Flint, S.S. and Hodgson, D.M. (2016) Decoupling seasonal fluctuations in fluvial discharge from the tidal signature in ancient deltaic deposits: an example from the Neuquén Basin, Argentina. *J. Geol. Soc. London*, **173,** 94-107.
Hadley, D.F., Arochukwu, E.C., Nishi, K., Sarginson, M.J., Salleh, H. and Omar, M. (2006) Depositional Modelling of Champion Field, Brunei. In: *Society of Petroleum Engineers Asia Pacific Oil and Gas Conference and Exhibition*. Society of Petroleum Engineers, Adelaide, Australia.
Hall, R. (2002) Cenozoic geological and plate tectonic evolution of SE Asia and the SW Pacific: computer-based reconstructions, model and animations. *J. Asian Earth Sci.*, **20,** 353-431.
Hall, R. (2012) Late Jurassic–Cenozoic reconstructions of the Indonesian region and the Indian Ocean. *Tectonophysics*, **570-571,** 1-41.
Hall, R. (2013) The palaeogeography of Sundaland and Wallacea since the Late Jurassic. *J. Limnol.*, **72,** 1-17.
Hall, R., Ali, J.R., Anderson, C.D. and Baker, S.J. (1995) Origin and motion history of the Philippine Sea Plate. *Tectonophysics*, **251,** 229-250.
Hanebuth, T.J., Stattegger, K., Schimanski, A., Lüdmann, T. and Wong, H.K. (2003) Late Pleistocene forced-regressive deposits on the Sunda Shelf (Southeast Asia). *Mar. Geol.*, **199,** 139-157.
Hanebuth, T.J., Voris, H.K., Yokoyama, Y., Saito, Y. and Okuno, J.i. (2011) Formation and fate of

sedimentary depocentres on Southeast Asia's Sunda Shelf over the past sea-level cycle and biogeographic implications. *Earth-Science Reviews*, **104,** 92-110.
Harms, J.C., Southard, J.B. and Walker, R.G. (1982) *Structures and Sequences in Clastic Rocks*. SEPM, Tulsa, Oklahoma, 249 pp.
Harris, P.T., Heap, A.D., Bryce, S.M., Porter-Smith, R., Ryan, D.A. and Heggie, D.T. (2002) Classification of Australian Clastic Coastal Depositional Environments Based Upon a Quantitative Analysis of Wave, Tidal, and River Power. *J. Sed. Res.*, **72,** 858-870.
Hazebroek, H.P. and Tan, D.N.K. (1993) Tectonic evolution of the NW Sabah continental margin since the Late Eocene. In: *Proceedings symposium on the Tectonic framework and energy resources of the western margin of the Pacific Basin* (Ed G.H. Teh), *Special Publication*, **33**, pp. 195–210. Geological Society of Malaysia, Kuala Lumpur.
Hinz, K., Fritsch, J., Kempter, E., Mohammad, M.A.M., Meyer, J., Mohamed, M.D., Vosberg, D.G.H., Weber, D.I.J. and Benavidez, M.J. (1989) Thrust tectonics along the north-western continental margin of Sabah/Borneo. *Geol. Rundsch.*, **78,** 705-730.
Hjulström, F. (1939) Transportation of Debris by Moving Water. In: *Recent Marine Sediments* (Ed P.D. Trask), pp. 5-31. AAPG, Tulsa, OK.
Holloway, N.H. (1982) North Palawan block, Philippines--Its relation to Asian mainland and role in evolution of South China Sea. *AAPG Bull.*, **66,** 1355-1383.
Hori, H. (2000) *The Mekong: environment and development*. United Nations University Press, Tokyo, 398 pp.
Howarth, M.J. (1982) Tidal currents of the continental shelf. In: *Offshore Tidal Sands: Processes and Deposits* (Ed A.H. Stride), pp. 10-26. Chapman & Hall, London.
Huang, B., Xiao, X. and Li, X. (2003) Geochemistry and origins of natural gases in the Yinggehai and Qiongdongnan basins, offshore South China Sea. *Org. Geochem.*, **34,** 1009-1025.
Hutchison, C.S. (2005) *Geology of North-West Borneo: Sarawak, Brunei and Sabah*. Elsevier, Amsterdam, 444 pp.
Hutchison, C.S. (2010) The North-West Borneo Trough. *Mar. Geol.*, **271,** 32-43.
Immenhauser, A. (2009) Estimating palaeo-water depth from the physical rock record. *Earth-Science Reviews*, **96,** 107-139.
Ingram, G.M., Chisholm, T.J., Grant, C.J., Hedlund, C.A., Stuart-Smith, P. and Teasdale, J. (2004) Deepwater North West Borneo: hydrocarbon accumulation in an active fold and thrust belt. *Mar. Pet. Geol.*, **21,** 879-887.
Jardine, E. (1997) Dual petroleum systems governing the prolific Pattani Basin, offshore Thailand. In: *International Conference on Petroleum Systems of SE Asia and Australasia, Indonesian Petroleum Association* (Eds J.V.C. Howes and R.A. Noble), pp. 351-363, Jakarta, Indonesia.
Julien, P.Y. and Raslan, Y. (1998) Upper-regime plane bed. *J. Hydraul. Eng.*, **124,** 1086-1096.
Kowalik, Z. and Luick, J. (2013) *The Oceanography of Tides*. University of Alaska Fairbanks, Fairbanks, Alaska, 157 pp.
Kowalik, Z. and Murty, T.S. (1993) *Numerical modeling of ocean dynamics*. World Scientific, Singapore, 481 pp.
Kvale, E.P. (2012) Tidal constituents of modern and ancient tidal rhythmites: criteria for recognition and analyses. In: *Principles of Tidal Sedimentology* (Eds R.A. Davis and R.W. Dalrymple), pp. 1-17. Springer, New York.
Lambiase, J.J., bin Abdul Rahim, A.A. and Peng, C.Y. (2002) Facies distribution and sedimentary processes on the modern Baram Delta: implications for the reservoir sandstones of NW Borneo. *Mar. Pet. Geol.*, **19,** 69-78.
Lambiase, J.J., Damit, A.R., Simmons, M.D., Abdoerrias, R. and Hussin, A. (2003) A depositional model and the stratigraphic development of modern and ancient tide-dominated deltas in NW Borneo. In: *Tropical Deltas of Southeast Asia – Sedimentology, Stratigraphy, and Petroleum Geology* (Eds F.H. Sidi, D. Nummedal, P. Imbert, H. Darman and H.W. Posamentier), *Special Publication 76*, pp. 109-123. SEPM.

Lee, G.H., Lee, K. and Watkins, J.S. (2001) Geologic evolution of the Cuu Long and Nam Con Son basins, offshore southern Vietnam, South China Sea. *AAPG Bull.*, **85,** 1055-1082.
Lee, G.H. and Watkins, J.S. (1998) Seismic sequence stratigraphy and hydrocarbon potential of the Phu Khanh Basin, offshore central Vietnam, South China Sea. *AAPG Bull.*, **82,** 1711-1735.
Legler, B., Johnson, H.D., Hampson, G.J., Massart, B.Y.G., Jackson, C.A.L., Jackson, M.D., El-Barkooky, A. and Ravnås, R. (2013) Facies model of a fine-grained, tide-dominated delta: Lower Dir Abu Lifa Member (Eocene), Western Desert, Egypt. *Sedimentology*, **60,** 1313-1356.
Levell, B.K. (1987) The nature and significance of regional unconformities in the hydrocarbon-bearing Neogene sequences offshore West Sabah. *Geol. Soc. Malaysia Bull.*, **21,** 55-90.
Li, M., Wang, T., Liu, J., Lu, H., Wu, W. and Gao, L. (2008) Occurrence and origin of carbon dioxide in the Fushan Depression, Beibuwan Basin, South China Sea. *Mar. Pet. Geol.*, **25,** 500-513.
Li, Z., Saito, Y., Mao, L., Tamura, T., Song, B., Zhang, Y., Lu, A., Sieng, S. and Li, J. (2012) Mid-Holocene mangrove succession and its response to sea-level change in the upper Mekong River delta, Cambodia. *Quat. Res.*, **78,** 386-399.
Lockhart, B.E., Chinoroje, O., Enomoto, C.B. and Hollomon, G.A. (1997) Early Tertiary deposition in the southern Pattani Trough, Gulf of Thailand. In: *The International Conference on Stratigraphy and Tectonic Evolution of Southeast Asia and the South Pacific* (Eds P. Dheeradilok, C. Hinthong, P. Chaodumrong, P. Putthaphiban, W. Tansathien, C. Utha-aroon, N. Sattyarak, T. Nuchanong and S. Techawan), pp. 476-489, Bangkok, Thailand.
Longhitano, S.G., Mellere, D., Steel, R.J. and Ainsworth, R.B. (2012) Tidal depositional systems in the rock record: A review and new insights. *Sediment. Geol.*, **279,** 2-22.
Longley, I.M. (1997) The tectonostratigraphic evolution of SE Asia. In: *Petroleum Geology of Southeast Asia* (Eds A.J. Fraser, S.J. Matthews and R.W. Murphy), *Special Publications*, **126**, pp. 311-339. Geological Society London, London, UK.
MacEachern, J.A. and Bann, K.L. (2008) The role of ichnology in refining shallow marine facies models. In: *Recent Advances in Models of Siliciclastic Shallow-Marine Stratigraphy* (Eds G.J. Hampson, R.J. Steel, P.M. Burgess and R.W. Dalrymple), *Special Publication 90*, pp. 73-116. SEPM.
Madon, M.B. (1999) North Luconia Province. In: *The Petroleum Geology and Resources of Malaysia* (Ed L.K. Meng), pp. 343-367. Petroliam Nasional Berhard (PETRONAS), Kuala Lumpur, Malaysia.
Madon, M.B., Abolins, P., Hoesni, M.J.B. and Ahmad, M.B. (1999) Malay Basin. In: *The Petroleum Geology and Resources of Malaysia* (Ed L.K. Meng), pp. 173-217. Petroliam Nasional Berhard (PETRONAS), Kuala Lumpur, Malaysia.
Madon, M.B. and Anuar, A. (1999) Penyu Basin. In: *The Petroleum Geology and Resources of Malaysia* (Ed L.K. Meng), pp. 219-234. Petroliam Nasional Berhard (PETRONAS), Kuala Lumpur, Malaysia.
Markwick, P.J. and Valdes, P.J. (2004) Palaeo-digital elevation models for use as boundary conditions in coupled ocean–atmosphere GCM experiments: a Maastrichtian (late Cretaceous) example. *Palaeogeog. Palaeoclimatol. Palaeoecol.*, **213,** 37-63.
Martinius, A.W., Kaas, I., Næss, A., Helgesen, G., Kjærefjord, J.M. and Leith, D.A. (2001) Sedimentology of the heterolithic and tide-dominated tilje formation (Early Jurassic, Halten Terrace, Offshore Mid-Norway). In: *Norwegian Petroleum Society* (Eds J.M. Ole and D. Tom), *Special Publications*, **10**, pp. 103-144. Elsevier.
Martinius, A.W. and Van den Berg, J.H. (2011) *Atlas of sedimentary structures in estuarine and tidally-influenced river deposits of the Rhine-Meuse-Scheldt system*. EAGE Publications BV, Houten, 298 pp.
Matthews, S.J., Fraser, A.J., Lowe, S., Todd, S.P. and Peel, F.J. (1997) Structure, stratigraphy and petroleum geology of the SE Nam Con Son Basin, offshore Vietnam. In: *Petroleum Geology of Southeast Asia* (Eds A.J. Fraser, S.J. Matthews and R.W. Murphy), *Special Publications*, **126**, pp. 89-106. Geological Society London, London, UK.
Mazlan, M. (1999) Geological setting of Sarawak. In: *The Petroleum Geology and Resources of Malaysia* (Ed L.K. Meng), pp. 275-290. Petroliam Nasional Berhard (PETRONAS), Kuala Lumpur,

Malaysia.
Mazur, S., Green, C., Stewart, M.G., Whittaker, J.M., Williams, S. and Bouatmani, R. (2012) Displacement along the Red River Fault constrained by extension estimates and plate reconstructions. *Tectonics*, **31,** TC5008.
Miall, A.D. (2015) Updating uniformitarianism: stratigraphy as just a set of 'frozen accidents'. In: *Strata and Time: Probing the Gaps in Our Understanding* (Eds D.G. Smith, R.J. Bailey, P.M. Burgess and A.J. Fraser), *Special Publication 404*, **404**, pp. 11-36. Geological Society of London.
Miller, K.G., Mountain, G.S., Wright, J.D. and Browning, J.V. (2011) A 180-Million-Year Record of Sea Level and Ice Volume Variations from Continental Margin and Deep-Sea Isotopic Records. *Oceanography*, **24,** 40-53.
Miller, M.C., McCave, I.N. and Komar, P.D. (1977) Threshold of sediment motion under unidirectional currents. *Sedimentology*, **24,** 507-527.
Mitchell, A.J., Allison, P.A., Gorman, G.J., Piggott, M.D. and Pain, C.C. (2011) Tidal circulation in an ancient epicontinental sea: The Early Jurassic Laurasian Seaway. *Geology*, **39,** 207-210.
Mitchell, A.J., Uličný, D., Hampson, G.J., Allison, P.A., Gorman, G.J., Piggott, M.D., Wells, M.R. and Pain, C.C. (2010) Modelling tidal current-induced bed shear stress and palaeocirculation in an epicontinental seaway: the Bohemian Cretaceous Basin, Central Europe. *Sedimentology*, **57,** 359-388.
Mohammad Yamin, A. and Abolins, P. (1999) Central Luconia Province. In: *The Petroleum Geology and Resources of Malaysia* (Ed L.K. Meng), pp. 371–392. Petroliam Nasional Berhard (PETRONAS), Kuala Lumpur, Malaysia.
Morley, C.K. (2012) Late Cretaceous–Early Palaeogene tectonic development of SE Asia. *Earth Sci. Rev.*, **115,** 37-75.
Morley, C.K. (2016) Major unconformities/termination of extension events and associated surfaces in the South China Seas: Review and implications for tectonic development. *J. Asian Earth Sci.*, **120,** 62-86.
Morley, R.J., Morley, H.P. and Restrepo-Pace, P. (2003) Unravelling the tectonically controlled stratigraphy of the west Natuna Basin by means of palaeo-derived Mid Tertiary climate changes.
Morley, R.J., Swiecicki, T. and Pham, D.T.T. (2011) A sequence stratigraphic framework for the Sunda region, based on integration of biostratigraphic, lithological and seismic data from Nam Con Son basin, Vietnam. In: *Indonesian Petroleum Association 35th Annual Convention*, pp. IPA11-G-002, Jakarta, Indonesia.
Müller, R.D., Roest, W.R., Royer, J.Y., Gahagan, L.M. and Sclater, J.G. (1997) Digital isochrons of the world's ocean floor. *J. Geophys. Res.*, **102,** 3211-3214.
Nio, S.-D. and Yang, C.-S. (1991) Diagnostic attributes of clastic tidal deposits: a review. In: *Clastic Tidal Sedimentology* (Eds D. Smith, G.G.E. Reinson, B.A. Zaitlin and R.A. Rahmani), pp. 3-27. Canadian Society of Petroleum Geologists, Memoir 16.
Nyberg, B. and Howell, J.A. (2016) Global distribution of modern shallow marine shorelines. Implications for exploration and reservoir analogue studies. *Mar. Pet. Geol.*, **71,** 83-104.
Olariu, C., Steel, R.J., Dalrymple, R.W. and Gingras, M.K. (2012) Tidal dunes versus tidal bars: The sedimentological and architectural characteristics of compound dunes in a tidal seaway, the lower Baronia Sandstone (Lower Eocene), Ager Basin, Spain. *Sediment. Geol.*, **279,** 134-155.
Open University Course Team (1999) *Waves, Tides and Shallow-water Processes: Second Edition*. Butterworth-Heinemann, Oxford, UK, 227 pp.
Pietrzak, J., Jakobson, J.B., Burchard, H., Vested, H.J. and Petersen, O. (2002) A three-dimensional hydrostatic model for coastal and ocean modelling using a generalised topography following co-ordinate system. *Ocean Modelling*, **4,** 173-205.
Piggott, M.D., Gorman, G.J., Pain, C.C., Allison, P.A., Candy, A.S., Martin, B.T. and Wells, M.R. (2008) A new computational framework for multi-scale ocean modelling based on adapting unstructured meshes. *Int. J. Numer. Meth. Fluids*, **56,** 1003-1015.
Pingree, R.D. and Griffiths, D.K. (1979) Sand transport paths around the British Isles resulting from

M2 and M4 tidal interactions. *J. Mar. Biol. Assoc. UK*, **59,** 497-513.
Piper, D.J., Kontopoulos, N., Anagnostou, C., Chronis, G. and Panagos, A. (1990) Modern fan deltas in the western Gulf of Corinth, Greece. *Geo-Mar. Lett.*, **10,** 5-12.
Plink-Björklund, P. (2012) Effects of tides on deltaic deposition: Causes and responses. *Sediment. Geol.*, **279,** 107-133.
Plotnick, R.E. (1986) A fractal model for the distribution of stratigraphic hiatuses. *J. Geol.*, **94,** 885-890.
Posamentier, H.W. and Allen, G.P. (1999) *Siliciclastic sequence stratigraphy: concepts and applications*. SEPM, Tulsa, OK, 210 pp.
Redfield, A.C. (1958) The influence of the continental shelf on the tides of the Atlantic coast of the United States. *J. Mar. Res.*, **17,** 432-448.
Replumaz, A. and Tapponnier, P. (2003) Reconstruction of the deformed collision zone between India and Asia by backward motion of lithospheric blocks. *J. Geophys. Res.*, **108,** B62285.
Rossi, V.M. and Steel, R.J. (2016) The role of tidal, wave and river currents in the evolution of mixed-energy deltas: Example from the Lajas Formation (Argentina). *Sedimentology*, **63,** 824–864.
Rubin, D.M. and McCulloch, D.S. (1980) Single and superimposed bedforms: a synthesis of San Francisco Bay and flume observations. *Sediment. Geol.*, **26,** 207-231.
Sadler, P.M. (1981) Sediment accumulation rates and the completeness of stratigraphic sections. *J. Geol.*, **89,** 569-584.
Safak, I. (2016) Variability of Bed Drag on Cohesive Beds under Wave Action. *Water*, **8,** 131.
Sandal, S.T. (1996) *The Geology and Hydrocarbon Resources of Negara Brunei Darussalam*. Brunei Shell Petroleum Company, Brunei Museum, Bandar Seri Begawan, Brunei Darussalam, 243 pp.
Shamsudin, J. and Morley, R.J. (2006) Integrating Biostratigraphy with Seismic for Sequence Stratigraphic Interpretation in The Malay Basin. In: *PGCE 2006*, pp. 101-102.
Shoup, R.C., Morley, R.J., Swiecicki, T. and Clark, S. (2013) Tectono-stratigraphic Framework and Tertiary Paleogeogeography of Southeast Asia; Gulf of Thailand to South Vietnam Shelf. *Hou. Geol. Soc. Bull.*, **55,** 27-39.
Simons, W.J.F., Socquet, A., Vigny, C., Ambrosius, B.A.C., Haji Abu, S., Promthong, C., Subarya, C., Sarsito, D.A., Matheussen, S., Morgan, P. and Spakman, W. (2007) A decade of GPS in Southeast Asia: Resolving Sundaland motion and boundaries. *J. Geophys. Res.*, **112,** B06420.
Slingerland, R. (1986) Numerical computation of co-oscillating palaeotides in the Catskill epeiric Sea of eastern North America. *Sedimentology*, **33,** 487-497.
Soulsby, R., Hamm, L., Klopman, G., Myrhaug, D., Simons, R. and Thomas, G. (1993) Wave-current interaction within and outside the bottom boundary layer. *Coastal Eng.*, **21,** 41-69.
Steel, R.J., Plink-Bjorklund, P. and Aschoff, J. (2012) Tidal deposits of the Campanian Western Interior Seaway, Wyoming, Utah and Colorado, USA. In: *Principles of Tidal Sedimentology* (Eds R.A. Davies and R.W. Dalrymple), pp. 437-471. Springer-Verlag, New York.
Stein, C.A. and Stein, S. (1992) A model for the global variation in oceanic depth and heat flow with lithospheric age. *Nature*, **359,** 123-129.
Storms, J.E.A. (2003) Event-based stratigraphic simulation of wave-dominated shallow-marine environments. *Mar. Geol.*, **199,** 83-100.
Stride, A.H. (1973) Sediment transport by the North Sea. In: *North Sea Science* (Ed E.D. Goldberg), pp. 101-130. MIT Press, Cambridge, MA.
Suzuki, S., Takemura, S., Yumul, G.P., David, S.D. and Asiedu, D.K. (2000) Composition and provenance of the Upper Cretaceous to Eocene sandstones in Central Palawan, Philippines: Constraints on the tectonic development of Palawan. *Isl. Arc*, **9,** 611-626.
Tamura, T., Saito, Y., Sieng, S., Ben, B., Kong, M., Sim, I., Choup, S. and Akiba, F. (2009) Initiation of the Mekong River delta at 8 ka: evidence from the sedimentary succession in the Cambodian lowland. *Quat. Sci. Rev.*, **28,** 327-344.
Tapponnier, P., Peltzer, G. and Armijo, R. (1986) On the mechanics of the collision between India and Asia. In: *Collision Tectonics* (Eds M.P. Coward and A.C. Ries), *Special Publications*, **19**, pp. 113-

157. Geological Society, London, London, UK.
Taylor, B. and Hayes, D.E. (1983) Origin and History of the South China Sea Basin. In: *The Tectonic and Geologic Evolution of Southeast Asian Seas and Islands: Part 2* (Ed D.E. Hayes), *Geophysical Monograph*, **27**, pp. 23-56. American Geophysical Union, Washington, D.C.
Thorne, J.A., Grace, E., Swift, D.J.P. and Niedoroda, A. (1991) Sedimentation on Continental Margins, III: The depositional fabric—an analytical approach to stratification and facies identification. In: *Shelf Sand and Sandstone Bodies: Geometry, Facies and Sequence Stratigraphy* (Eds D.J.P. Swift, G.F. Oertel, R.W. Tillman and J.A. Thorne), *Special Publication 14*, **14**, pp. 59-87. IAS.
Tin, N.T. and Ty, N.D. (1995) Petroleum geology of the Nam Con Son Basin. *Geol. Soc. Malaysia Bull.*, **37,** 1-11.
Tsuchi, R. (1997) Marine climatic responses to Neogene tectonics of the Pacific Ocean seaways. *Tectonophysics*, **281,** 113-124.
Vakarelov, B.K. and Ainsworth, R.B. (2013) A hierarchical approach to architectural classification in marginal-marine systems: Bridging the gap between sedimentology and sequence stratigraphy. *AAPG Bull.*, **97,** 1121-1161.
Vakarelov, B.K., Ainsworth, R.B. and MacEachern, J.A. (2012) Recognition of wave-dominated, tide-influenced shoreline systems in the rock record: Variations from a microtidal shoreline model. *Sediment. Geol.*, **279,** 23-41.
van Cappelle, M., Ravnås, R., Hampson, G.J. and Johnson, H.D. (2017) Depositional evolution of a progradational to aggradational, mixed-influenced deltaic succession: Jurassic Tofte and Ile formations, southern Halten Terrace, offshore Norway. *Mar. Pet. Geol.*, **80,** 1-22.
van Cappelle, M., Stukins, S., Hampson, G.J. and Johnson, H.D. (2016) Fluvial to tidal transition in proximal, mixed tide-influenced and wave-influenced deltaic deposits: Cretaceous lower Sego Sandstone, Utah, USA. *Sedimentology*, **63,** 1333–1361.
van Hattum, M.W.A., Hall, R., Pickard, A.L. and Nichols, G.J. (2006) Southeast Asian sediments not from Asia: Provenance and geochronology of north Borneo sandstones. *Geology*, **34,** 589.
Van Wagoner, J.C. (1991) High-frequency sequence stratigraphy and facies architecture of the Sego Sandstone in the Book Cliffs of western Colorado and eastern Utah. In: *Sequence Stratigraphy—Applications to Shelf Sandstone Reservoirs Outcrop to Subsurface Examples* (Eds J.C. Van Wagoner, D. Nummedal, C.R. Jones, D.R. Taylor, D.C. Jennette and G.W. Riley), *AAPG Field Conference Guidebook*, pp. 1–22.
Weatherall, P., Marks, K., Jakobsson, M., Schmitt, T., Tani, S., Arndt, J.E., Rovere, M., Chayes, D., Ferrini, V. and Wigley, R. (2015) A new digital bathymetric model of the world's oceans. *Earth and Space Science*, **2,** 331-345.
Wells, M.R. (2008) *Tidal modelling of modern and ancient seas and oceans*, Imperial College London, 527 pp.
Wells, M.R., Allison, P.A., Hampson, G.J., Piggott, M.D. and Pain, C.C. (2005a) Modelling ancient tides: the Upper Carboniferous epi-continental seaway of Northwest Europe. *Sedimentology*, **52,** 715-735.
Wells, M.R., Allison, P.A., Piggott, M.D., Gorman, G.J., Hampson, G.J., Pain, C.C. and Fang, F. (2007a) Numerical Modeling of Tides in the Late Pennsylvanian Midcontinent Seaway of North America with Implications for Hydrography and Sedimentation. *J. Sed. Res.*, **77,** 843-865.
Wells, M.R., Allison, P.A., Piggott, M.D., Hampson, G.J., Pain, C.C. and Gorman, G.J. (2010a) Tidal Modeling of an Ancient Tide-Dominated Seaway, Part 1: Model Validation and Application to Global Early Cretaceous (Aptian) Tides. *J. Sed. Res.*, **80,** 393-410.
Wells, M.R., Allison, P.A., Piggott, M.D., Hampson, G.J., Pain, C.C. and Gorman, G.J. (2010b) Tidal Modeling of an Ancient Tide-Dominated Seaway, Part 2: The Aptian Lower Greensand Seaway of Northwest Europe. *J. Sed. Res.*, **80,** 411-439.
Wells, M.R., Allison, P.A., Piggott, M.D., Pain, C.C., Hampson, G.J. and De Oliveira, C.R. (2005b) Large sea, small tides: the Late Carboniferous seaway of NW Europe. *J. Geol. Soc.*, **162,** 417-420.
Wells, M.R., Allison, P.A., Piggott, M.D., Pain, C.C., Hampson, G.J. and Dodman, A. (2007b)

Investigating tides in the Early Pennsylvanian Seaway of NW Eurasia using the Imperial College Ocean Model. In: *Dynamics of Epeiric Seas: Sedimentological, Paleontological and Geochemical Perspectives* (Eds C. Holmden and B.R. Pratt), *Special Paper 48*, pp. 363-387. Geological Association of Canada.
Wheatcroft, R.A. and Drake, D.E. (2003) Post-depositional alteration and preservation of sedimentary event layers on continental margins, I. The role of episodic sedimentation. *Mar. Geol.*, **199,** 123-137.
Wolanski, E.E.J., Mazda, Y.Y. and Ridd, P.P.V. (1992) Mangrove hydrodynamics. In: *Tropical Mangrove Ecosystems* (Eds A.I. Robertson and D.M. Alongi), *Coastal and Estuarine Studies*, **41**, pp. 43-62. American Geophysical Union, Washington, DC.
Woodroffe, C.D., Rogers, K., McKee, K.L., Lovelock, C.E., Mendelssohn, I.A. and Saintilan, N. (2016) Mangrove sedimentation and response to relative sea-level rise. *Ann Rev Mar Sci*, **8,** 243-66.
Yoshida, S., Steel, R.J. and Dalrymple, R.W. (2007) Changes in depositional processes—an ingredient in a new generation of sequence-stratigraphic models. *J. Sed. Res.*, **77,** 447-460.
Zheng, W. and Deng, H. (2012) The Tidal Sandstone Characteristic of the Zhuhai Formation, Huizhou Oil Field, Pearl River Mouth Basin, South China Sea. *Pet Sci Technol*, **30,** 567-574.
Zhu, W., Huang, B., Mi, L., Wilkins, R.W.T., Fu, N. and Xiao, X. (2009) Geochemistry, origin, and deep-water exploration potential of natural gases in the Pearl River Mouth and Qiongdongnan basins, South China Sea. *AAPG Bull.*, **93,** 741-761.
Zhuo, H., Wang, Y., Shi, H., Zhu, M., He, M., Chen, W. and Li, H. (2014) Seismic geomorphology, architecture and genesis of Miocene shelf sand ridges in the Pearl River Mouth Basin, northern South China Sea. *Mar. Pet. Geol.*, **54,** 106-122.

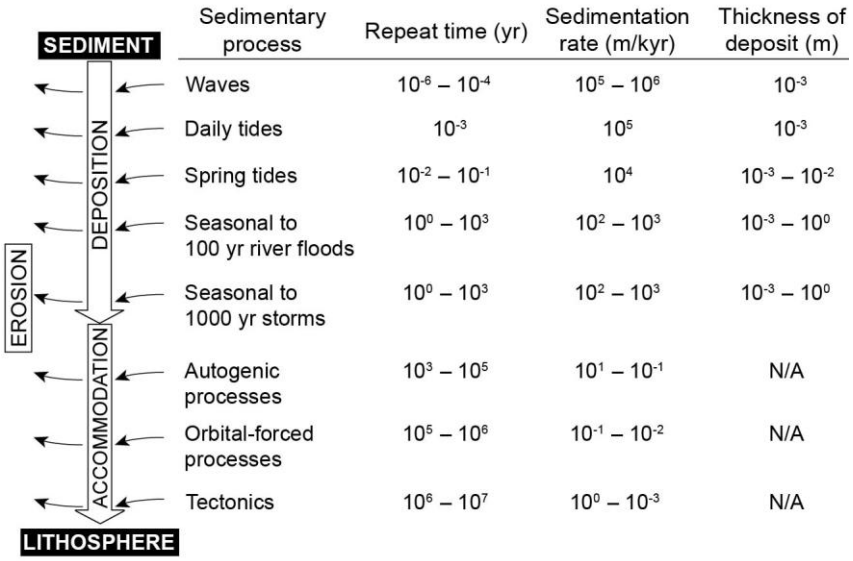

Sedimentary process	Repeat time (yr)	Sedimentation rate (m/kyr)	Thickness of deposit (m)
Waves	10^{-6} – 10^{-4}	10^{5} – 10^{6}	10^{-3}
Daily tides	10^{-3}	10^{5}	10^{-3}
Spring tides	10^{-2} – 10^{-1}	10^{4}	10^{-3} – 10^{-2}
Seasonal to 100 yr river floods	10^{0} – 10^{3}	10^{2} – 10^{3}	10^{-3} – 10^{0}
Seasonal to 1000 yr storms	10^{0} – 10^{3}	10^{2} – 10^{3}	10^{-3} – 10^{0}
Autogenic processes	10^{3} – 10^{5}	10^{1} – 10^{-1}	N/A
Orbital-forced processes	10^{5} – 10^{6}	10^{-1} – 10^{-2}	N/A
Tectonics	10^{6} – 10^{7}	10^{0} – 10^{-3}	N/A